Temperature-dependent stability of θ'-Al_2Cu precipitates investigated with Phase Field simulations and experiments

Patrick Shower[1,2], James R. Morris[1,3], Dongwon Shin[1], Balasubramaniam Radhakrishnan[4], Lawrence L. Allard[1], Amit Shyam[1,2]

1. *Materials Science and Technology Division, Oak Ridge National Laboratory, Oak Ridge, TN*
2. *The Bredesen Center for Interdisciplinary Research and Graduate Education, University of Tennessee, Knoxville, TN*
3. *Department of Materials Science and Engineering, The University of Tennessee, Knoxville, TN*
4. *Computational Sciences and Engineering Division, Oak Ridge National Laboratory, Oak Ridge, TN*

Abstract

The upper limit of service temperature for many Al-Cu alloys is determined by the thermal stability of strengthening θ′ (Al_2Cu) precipitates. Above a certain temperature, θ′ precipitates will undergo morphological evolution and transform into the detrimental, equilibrium θ phase, leading to a rapid drop in strength. Certain alloying elements have recently been reported to increase the thermal stability of θ′ precipitates, by mechanisms that are yet unclear. Herein, we investigate the effect of modified interfacial energy and solute chemical mobility on the thermal stability of θ′ *via* high-throughput phase field study. We identify a critical θ′ aspect ratio to predict the onset of θ formation. Using this criterion, we predict the time required for θ′ to θ phase transformation as a function of temperature, Cu diffusivity, and the interfacial energy of θ′ precipitates. The predicted times compare favorably with reported times for θ formation under similar experimental conditions. These phase field simulations predict that a moderate reduction in Cu mobility or matrix-precipitate interfacial energy is adequate to stabilize the as-aged microstructure up to 300 °C, while substantial reductions to both interfacial energy and Cu mobility are needed to achieve similar stability at 400 °C. Experimental microstructural evolution results in commercial (319) and thermally stabilized (RR350) cast aluminum alloys are presented to complement the simulations.

Keywords: Al-Cu alloys; θ′-Al_2Cu; Phase field simulation; Coarsening; Kinetics

1. Introduction

The mechanical properties of precipitate strengthened Al-Cu-(Si) alloys depend heavily on the volume fraction, number density, and aspect ratio of the strengthening precipitates [1]. At elevated homologous temperatures ($T/T_{Melt} > 0.5$), the number density and aspect ratio of precipitates in these alloys tend to decrease due to coarsening (Ostwald ripening and shape evolution) [2, 3]. For many commercial cast Al-Cu and Al-Si-Cu alloys, the primary strengthening precipitates are disc-shaped particles of the metastable θ′ phase (body centered tetragonal Al_2Cu, a=4.04 Å and c=5.80 Å) [4]. The as-aged microstructures in these alloys are populated by θ′ precipitates with a high number density and average aspect ratio (diameter/thickness) in the range of 25-50 [5]. Above approximately 200 °C, the as-aged microstructure of these alloys deteriorates over time as θ′ particles rapidly coarsen [2-4, 6-8]. As larger particles grow at the expense of smaller particles, individual particles also undergo shape evolution, reducing their aspect ratio [5, 9]. Eventually, this morphological evolution leads to a phase transformation as the detrimental, equilibrium θ phase (tetragonal Al_2Cu) nucleates on coarsened, low aspect ratio θ′ particles [5, 10, 11]. The formation of the θ phase further accelerates the coarsening process because it has high-energy, incoherent interfaces with the Al matrix [12, 13]. The θ phase may coarsen at the expense of finer θ′ particles, and the mechanical properties of the alloy deteriorate substantially following this phase transformation (~60% reduction in strength and hardness) [3, 4, 14, 15]. The reduced mechanical properties limit the usefulness of many cast Al-Cu-(Si) alloys at elevated temperatures [16].

It is, therefore, desirable to develop alloys in which the onset of θ′ to θ transformation is delayed or prevented at elevated temperatures. Such high temperature stabilization of θ′ has been recently reported: The addition of Mn and Zr to an Al-Cu alloy, along with suppressed Si content, results in a θ′ strengthened microstructure which is morphologically stable to a temperature of at least 350 °C [6, 14]. Mechanisms have been proposed to explain the thermal stability of these alloys (termed *ACMZ* alloys hereafter), but the extent to which the individual mechanism(s) account for the high temperature microstructural stability remains unclear. It is also reported that Mn and Zr both tend to segregate to the interfaces between θ′ and the aluminum matrix [6]. This suggests that Mn and/or Zr might reduce the interfacial energy of θ′, which would lower the thermodynamic driving force for particle coarsening [5, 6, 17]. It is also plausible that Mn and/or Zr atoms could provide a kinetic barrier, inhibiting the diffusion of Cu atoms to and from θ′ particles [6, 18, 19].

The relative importance of kinetic versus interfacial thermodynamic mechanisms in stabilizing θ′ precipitates in ACMZ alloys is difficult to determine experimentally. Phase field simulations are, however, well suited for such an investigation. Phase field simulations have been successfully implemented to recreate microstructural phenomena in several materials systems (see reviews for various systems [20-24]), and in more recent years to guide materials design. In the case of the Al-Cu system, nucleation [25-29], growth [30, 31], shape evolution [32, 33], and coarsening [34, 35] processes associated with θ′ have been simulated and are in broad agreement with experimental results. Here, we use phase field modeling with comparison to experiment to evaluate the potential sources of the thermal stabilization phenomenon described above, with the intent of determining whether its nature is most likely thermodynamic, kinetic, or a combination of the two. The thermodynamic and kinetic effects of solute segregation are treated implicitly, using inputs from *ab initio* calculations and diffusivity databases, to provide specific information on the role of Cu diffusivity and matrix/θ′ interfacial free energy on the kinetics of coarsening. We examine the role of both thermodynamic and kinetic modifications in determining the morphological stability of Al-Cu microstructures, and describe how their relative importance varies with temperature.

The manuscript is organized as follows: In Section 2, we first introduce the phase field model used in the study and then describe how thermodynamic and kinetic modifications are implemented. We further describe what metrics are used to evaluate the evolution of the simulated microstructure. In Section 3, we show phase field results and compare them to prior analytical approaches, as well as experimental microstructures. In Section 4, we discuss the implications of these results on alloy design and the understanding of overaging in Al-Cu alloys.

2. Materials, Methods, and Modeling Rationale

In Section 2.1 below, we first describe our phase field model, and the parameters that we have chosen to model the development of the Al-Cu systems. Section 2.2 describes the choices of modified parameters for Cu diffusivity and interfacial energetics, chosen to examine the potential of such changes for stabilizing the microstructure. In Section 2.3, we describe the choice of initial microstructures, and how that was selected based on experimental observations. Section 2.4 describes a phenomenological approach for determining the “lifetime” of the preferable θ′ microstructure, based upon the θ′ aspect ratio. Finally, Section 2.5 describes the experimental methods necessary for comparison with the model.

2.1. Phase field formalism and input parameters for simulations

A two-dimensional phase field simulation of the Al-Cu system was implemented in the Multiphysics Object-Oriented Simulation Environment (MOOSE) framework [36]. Using analytical tools available in MOOSE, phase field formulations with demonstrated effectiveness in prior work [32-35] were augmented with inputs from density functional theory (DFT) calculations to account for new microstructural observations. The simulation included the solid solution α-Al matrix and the metastable θ′-Al_2Cu precipitate phase. The physical and chemical descriptors incorporated in the simulation included each phase's temperature- and composition-dependent bulk free energy, lattice constants, temperature-dependent stiffness tensors, and anisotropic interfacial energy, as well as the temperature-dependent mobility of Cu. The formulation and implementation of each of these descriptors are detailed below. First, the generic formulas are outlined, and then each term is described in more detail.

The phase field model seeks to simulate microstructural evolution on the premise that the microstructure will tend to evolve towards a lower free energy state. In these simulations, the evolution of local Cu concentration was dictated by the Cahn-Hilliard equation (Eq. 1) and the local phase evolution was governed by the Allen-Cahn formulation (Eq. 2) [20] given below.

$$\frac{\partial x_{Cu}}{\partial t} = \nabla \cdot M_{Cu} \nabla \frac{\delta F}{\delta x_{Cu}} \tag{1}$$

$$\frac{\partial \eta}{\partial t} = -L \frac{\delta F}{\delta \eta} \tag{2}$$

where x_{Cu} represents the mole fraction of Cu at a given mesh point, η is an order parameter that describes which phase is present at a given mesh point (η has a value of 0 for the α phase and 1 for the θ′ phase), M_{Cu} is the chemical mobility of Cu, and L is interfacial kinetic coefficient. F is the total free energy of the system. Equations 1 and 2 are linked by the free energy, which indicates that compositional and phase evolution are coupled. F is found using the following formulation:

$$F = \int_{Volume} \left(f_{bulk} + f_{gradient} + f_{lattice\ strain}\right) d(Volume) \tag{3}$$

where f_{bulk} describes the Gibbs free energy of each phase, $f_{gradient}$ describes energy associated with compositional gradients and interfaces between phases, and $f_{lattice\ strain}$ describes energy associated with elastic lattice strains. These quantities are all expressed in terms of energy per unit volume.

For each mesh point in the simulation, f_{bulk} is calculated using the following formula:

$$f_{bulk} = f_{\theta'}(x_{Cu}) \cdot g(\eta) + f_{\alpha}(x_{Cu}) \cdot \left(1 - g(\eta)\right) \tag{4}$$

where $f_{\theta'}$ is the bulk free energy of the θ′ phase, f_{α} is the bulk free energy of the α phase, and g is a switching function that smoothly transitions from a value of 0 in the α phase to 1 in the θ′ phase:

$$g(\eta) = 3 \cdot \eta^2 - 2 \cdot \eta^3 \tag{5}$$

This type of free energy construction (Eqs. 4 and 5) has been commonly used in prior phase field modeling of the Al-Cu system when only a single order parameter is required [37]. In models which have used multiple order parameters to describe the orientation variants of the θ′ phase (e.g. η1, η2, η3), additional functions are required to establish the energetic equivalence of each θ′ variant and the exclusivity of each variant (such that only one variant could be present at a given mesh location). The most common type of function is a Landau polynomial with multiple degenerate minima and symmetry operations, as described elsewhere [35]. Our model, however, only included a single order parameter, allowing us to utilize the more straightforward approach described by Chen [37]. Using the single order parameter, η, we used existing capabilities in the MOOSE framework to locally assign the correct Euler angle to the stiffness tensor, transformation strain, and interfacial energy anisotropy of θ′, as described later in this section.

To find $f_\alpha(x_{Cu})$ and $f_{\theta'}(x_{Cu})$, the molar Gibbs free energy of formation of each phase at temperatures and compositions of interest was obtained from the TCAL3 database as implemented in Thermo-Calc, as shown in Figure 1. $f_\alpha(x_{Cu})$ was calculated for Cu concentrations of 0% and 33 atomic%. Because the θ′ phase has a fixed stoichiometry, its free energy is captured in a single data point at each temperature.

[Figure 1 about here]

The inability to directly calculate the free energy of θ′ (a line compound) as a function of Cu composition presents a challenge in phase field simulations, which describe microstructures using continuously variable composition and order parameter fields [20]. This problem has been addressed by Chen *et al.*, who introduced parabolic fitting functions of raw free energy data that retain critical thermodynamic parameters including the driving force for phase transformation and equivalent chemical potential between θ′ and α [32-35]. This method [32] is used to derive parabolic functions describing the composition- and temperature-dependent bulk free energy of each phase. These functions are of the form shown in Eq. 6, with coefficients tabulated in Table 1.

$$f\ \left[\frac{ev}{nm^3}\right] = a \cdot {x_{Cu}}^6 - b \cdot {x_{Cu}}^5 + c \cdot {x_{Cu}}^4 - d \cdot {x_{Cu}}^3 + e \cdot {x_{Cu}}^2 - h \cdot x_{Cu} + j \tag{6}$$

[Table 1 about here]

Additionally, $f_\alpha(x_{Cu})$ and $f_{\theta'}(x_{Cu})$ at 400 °C are plotted in Figure 2.

[Figure 2 about here]

$f_{gradient}$ is also calculated for each mesh point in the simulation, using Eq. 7:

$$f_{gradient} = \frac{\kappa_\eta}{2} \cdot \left|\nabla_\eta\right|^2 + \frac{\kappa_{Cu}}{2} \cdot \left|\nabla_{x_{Cu}}\right|^2 \qquad (7)$$

Here, κ_η and κ_{Cu} are gradient coefficients related to the energy of phase interfaces and compositional gradients, respectively. The interfacial energy (γ) of θ′ precipitates was calculated using DFT calculations, as described elsewhere [6]. Interfacial energy was calculated separately for the coherent $(1\ 0\ 0)_\alpha||(1\ 0\ 0)_{\theta'}$ interface and the semi-coherent $(0\ 1\ 0)_\alpha||(0\ 1\ 0)_{\theta'}$ interface, and was assumed to be constant with respect to temperature. The gradient coefficient terms required by Eq. 7 were calculated from γ values using the method described by Kim *et al*. [32]. Because the excess energy at the simulated θ′ interfaces arises from a combination of parameters including κ_{Cu}, κ_η, and f_{bulk}, each of these must be accounted for in order to implement the desired values for γ. The relationship between these terms was derived by Cahn and Hilliard [38], and is applied to the α/θ′ system in Eq. 8 [32, 35]:

$$\gamma = 2 \cdot \int_{x_{Cu,\alpha}}^{x_{Cu,\theta'}} [\kappa_{Cu} \cdot \Delta f_{bulk}(x_{Cu})]^{\frac{1}{2}} \cdot \left[1 + \frac{\kappa_\eta}{\kappa_{Cu}} \cdot \left(\frac{d\eta}{dx_{Cu}}\right)^2\right]^{\frac{1}{2}} dx_{Cu} \qquad (8)$$

where $\Delta f_{bulk}(x_{Cu})$ is the difference between f_{bulk} at a given value of x_{Cu} (minimized with respect to the value of η using the switching function) and the common tangent construction between f_α and $f_{\theta'}$ at that composition, $\frac{d\eta}{dx_{Cu}}$ is the change in order parameter with respect to composition, calculated using the value of the order parameter that minimizes f_{bulk} at the given composition, $x_{Cu,\alpha}$ (the Cu content of α) is taken to be 0.0025, and $x_{Cu,\theta'}$ (the Cu content of θ′) is taken to be 0.33. Again following the approach outlined in Ref. [32], γ, $\Delta f_{bulk}(x_{Cu})$, and $\frac{d\eta}{dx_{Cu}}$ were calculated initially, leaving two unknown parameters, κ_{Cu} and κ_η. κ_{Cu} was then assigned the same value assumed in prior work [35], and finally κ_η was calculated using Eq. 8. κ_η was calculated separately for the coherent and semi-coherent interfaces. Because $\gamma_{coherent}$ and $\gamma_{semi-coherent}$ were assumed to be constant, and $\Delta f_{bulk}(x_{Cu})$ was relatively invariant with temperature, the calculated values of $\kappa_{\eta,coherent}$ and $\kappa_{\eta,semi-coherent}$ were also relatively invariant with temperature. In order to improve the model's simplicity and consistency, $\kappa_{\eta,coherent}$ and $\kappa_{\eta,semi-coherent}$ were assumed to be temperature-independent, and were assigned a single value based on the average of their values calculated at each temperature. The values of each interfacial parameter are given in Table 2.

[Table 2 about here]

To calculate κ_η values at interface orientations intermediate to the coherent and semi-coherent interfaces of θ′, a compound sinusoidal function was used to smoothly interpolate between $\kappa_{\eta,coherent}$ and $\kappa_{\eta,semi-coherent}$ as a function of interface orientation. This function is:

$$\kappa_\eta = 1.845 \cdot \cos(4\psi + 180^{\circ}) + 3.081 \cdot \sin(2\psi + 90^{\circ}) + 9.055 \tag{9}$$

where ψ denotes the angle of the interface normal relative to that of the semi-coherent interface. The resulting κ_η profile is shown in a Wulff plot format in Figure 3. For comparison, the κ_η profile produced by applying the prior methodology [32, 35] to the same interfacial energy values is also plotted. The smooth, continuous energy minima applied in the present study serve to improve computational efficiency in the MOOSE framework.

[Figure 3 about here]

The calculation of $f_{lattice\ strain}$ using the microelasticity theory of Khachaturyan *et al.* [39] within the MOOSE framework is described elsewhere [36, 40, 41]. The principal inputs to this calculation are the stiffness tensors of each phase and the lattice mismatch between them. The temperature-dependent stiffness tensors of α-Al and θ′ were taken from acoustic measurements in the literature [42, 43] and are provided in Table 3. The anisotropic lattice mismatch between the α and θ′ phases along each interface was calculated by Vaithyanathan *et al.* using DFT models [35]. These calculations yield a 0.7% (dilatational) misfit of the θ′ particle along the coherent interface and a -5.1% (contractional) misfit along the semicoherent interface. These misfit strains were adopted in the present study and assumed to be invariant with precipitate size, as applied by others [35]. Although this is a simplification, multiple DFT studies have suggested that neither coherent nor semi-coherent interfacial energy of θ′ vary significantly with precipitate size [37, 44].

[Table 3 about here]

The mobility of Cu (M_{Cu} in Eq. 1) was also calculated using the formula presented by Vaithyanathan *et al.* in their simulations of the α/θ′ system, given below [35]:

$$M_{Cu} = D_{o,Cu} \cdot e^{-\frac{Q_{diff,Cu}}{R \cdot T}} \cdot \{X_{Cu} - (X_{Cu})^2\} \tag{10}$$

where $D_{o,Cu}$ is the diffusional prefactor, $Q_{diff,Cu}$ is the activation energy for tracer diffusion of Cu in pure Al, R is the ideal gas constant, T is absolute temperature, and X_{Cu} is the overall molar composition of Cu in the alloy. Note that, in this approach, the mobility of Cu is independent of local Cu composition. The diffusional terms were taken from the literature [45] and X_{Cu} was set at 2.1 at.% (~4 wt. %) in the simulations to replicate the conventional cast aluminum alloy 319 [2]. The resultant mobility terms are given in the Table 4. L, the kinetic prefactor term related to the formation and dissolution of θ′, was calculated for each simulation by solving the series of temporal equations given by Vaithyanathan *et al*. [35].

[Table 4 about here]

In the MOOSE Framework, Eqs. 1 and 2 are discretely evaluated at each point on a Finite Element Mesh using residual equations in the weak form [46]. In the present study, the residual equations were solved at each time step using Newton's method in the PETSc software package. Adaptive time steps and mesh densities were used to maximize computational efficiency while meeting residual convergence criteria. Using increasing mesh densities, we found that the thickness of the coherent interface ($0.05<\eta<0.95$) converged to approximately 0.7 nm, while the thickness of the semicoherent interface converged to approximately 1.1 nm. Using the standard adaptive mesh capability in MOOSE, the local mesh point distribution becomes finer if the compositional or order parameter gradient between two mesh points is a certain degree higher than the average in the simulation. We adjusted that degree to ensure that the narrowest interface, the coherent interface, was populated by 3 to 5 mesh points. This required at least 4.29 mesh points per nm of interface. Thus, we utilized an adaptive mesh with a maximum, density of 6.4 mesh points per nm of interface.

2.2. Quantifying the Influence of Global Kinetic and Thermodynamic Parameters

Once a baseline model for the α/θ' system was established, a numerical experiment was designed to quantify the influence of interfacial thermodynamics and diffusion kinetics on microstructural stability. Specifically, the time required for a virtual α/θ' microstructure to evolve beyond a critical aspect ratio (as discussed in section 2.3 below) was measured as a function of temperature, Cu mobility, and the interfacial energy of θ'. To frame this approach differently, we used phase field simulations to quantify the thermodynamic and/or kinetic modifications necessary to stabilize the α/θ' microstructure at different temperatures. This strategy is described below.

Once a virtual microstructure was established, the effects of modifying the thermodynamic and kinetic parameters associated with interfacial energy and Cu diffusion, respectively, on that microstructure's evolution were quantified. Thermodynamic modifications were introduced in order to reduce the driving force for microstructural evolution, while kinetic modifications were introduced in order to impede the rate-limiting step for microstructural evolution. These modifications are not a direct simulation of the Mn and Zr segregation to the interface of θ′ that has been observed experimentally [6]. Instead, they are intended to capture the thermodynamic and kinetic effects that such solute segregation might produce.

Considering the high temperature coarsening of the α/θ′ microstructure, the interfacial energy of θ′ particles provides the primary thermodynamic driving force. Ostwald ripening and shape evolution take place concurrently, reducing interfacial free energy as the large number of small, high aspect ratio (25-50) θ′ particles in the as-aged microstructure evolve into fewer, larger θ′ particles with an aspect ratio closer to the low equilibrium value (2-5) [9, 32]. Within this system, the semi-coherent interface has a greater energy (due to its structural and chemical differences with the Al matrix) and mobility (due to the ledge mechanism by which θ′ grows) than the coherent interface and is largely determinant in coarsening behavior [5, 47]. The interfacial energy of the semi-coherent interface was, therefore, identified as the key global parameter controlling the system's thermodynamics. We introduced reductions in $\gamma_{\text{semi-coherent}}$ up to -25% (a value which recent DFT work suggests is reasonable for alloying additions of Mn and Zr [6, 17]), in increments of 5%, thereby implementing systematic interfacial thermodynamic modifications to the virtual microstructure. For each level of thermodynamic modification, $\kappa_{\text{semi-coherent}}$ was recalculated using Eq. 8 and Eq. 9 was refit to the new value (see Table 5 for values).

[Table 5 about here]

The kinetics of θ′ coarsening are volume diffusion controlled, limited by the mobility of Cu in the α-Al matrix [5, 19]. In order to simulate a rate-limiting step which might alter the mechanism of Cu diffusion (*e.g.* a diffusion barrier at the θ′ interface or the motion of di-vacancies or vacancy-solute clusters, as has been hypothesized for similar systems [18]), the activation energy for Cu diffusion ($Q_{diff,Cu}$ in Eq. 10) was increased by up to +25%, in 5% increments. For each level of kinetic modification, M_{Cu} was recalculated using Eq. 10 (see Table 4 for values).

With a baseline phase field model, 5 levels of thermodynamic modification, and 5 levels of kinetic modification, a 6x6 test matrix results, wherein there are 36 "simulated alloys" with modified interfacial energy and Cu mobility, each of which has a unique combination of thermodynamic and kinetic characteristics. These simulated alloys were held at various simulated temperatures to observe how their microstructures evolved. By using several simulated alloys with varying degrees of kinetic and thermodynamic modification, this approach sidesteps the need for precise knowledge of solute element characteristics while determining the sensitivity of the virtual microstructure to these parameters. We expect that this method would be generally effective in developing a high-level understanding of which physical factors are most crucial in producing a microstructural evolution phenomenon of interest.

2.3. Initial Microstructure and Simulation Conditions

We reproduce the morphology and distribution of θ′ precipitates in an as-aged 319 aluminum alloy microstructure (alloy composition and heat treatment described elsewhere [2, 3, 14]) to create an initial *virtual microstructure*. 460 θ′ precipitates were imaged using high-angle annular dark-field (HAADF) scanning transmission electron microscopy (methods described in Section 2.4). A representative micrograph is shown in Figure 4a. The average number density of precipitates in the observation plane was determined to be 0.00008865 per nm^2 (as viewed along the $[100]_\alpha$ zone axis, neglecting precipitates with coherent faces parallel to the observation plane). This was implemented as 14 virtual particles populating a 397 nm x 397 nm α-Al matrix. The simulations were two dimensional, with θ′ precipitates modeled initially as rectangles (i.e. cross-sections of discs viewed edge-on). Two orthogonal orientation variants were used (excluding the third, in-plane variant which previous work suggests can only be accurately captured in a three dimensional mesh [30, 32, 35]), and 7 precipitates of each variant were included. The location of each precipitate was determined by a random number generator, under conditions that the precipitates intersected neither each other nor the simulation boundary. This method resulted in the virtual microstructure shown in Figure 4b. The simulation boundary was periodic with respect to all compositional and order parameter variables and the strain at each simulation boundary was held to zero. The thickness and diameter of the fourteen θ′ precipitates in the virtual microstructure were based on the distribution of measured precipitate dimensions. The measured and simulated dimensions are described in histograms (Figures 4c and 4d). For comparison to precipitate dimensions observed for other alloys and heat treatments, see elsewhere [48-51].

[Figure 4 about here]

The conditions of the phase field simulations were decided based on experimental observations. Given that conventional precipitate strengthened cast aluminum alloys are thermally destabilized above 200 °C while ACMZ alloys are thermally stable to at least 350 °C, the temperature range of interest was 100 °C to 400 °C, which we sampled in 100 °C increments. The simulations were run for 200 hours of physical time, corresponding to the industrial practice of preconditioning, in which cast aluminum alloys are held at temperature for 200 hours to evaluate the thermal stability of their microstructures [2, 3, 6, 15, 16]. The following expression [35] was used to relate simulated time (t^*) to physical time (t):

$$t^* = L \cdot |\Delta f| \cdot t \tag{11}$$

where $|\Delta f|$ is the maximum value of $\Delta f_{bulk}(x_{Cu})$.

2.4. *Aspect ratio of θ' as a metric of microstructural evolution*

To gauge microstructural stability as a function of temperature, kinetic modification, and thermodynamic modification, a metric of microstructural evolution must be defined. In this study, the particle aspect ratio was chosen as that metric. The aspect ratio of θ' particles has important implications for both the mechanical properties and microstructural evolution of precipitate strengthened Al-Cu alloys. For a given volume fraction and number density of θ' particles, the effectiveness of precipitate strengthening is diminished as average aspect ratio decreases during elevated temperature exposure [3, 12, 52]. Furthermore, the transformation of θ' into the equilibrium θ phase, which is detrimental to mechanical properties, is predicated by the aspect ratio of θ' particles reaching a critical value at which point the formation of incoherent θ particles becomes energetically favorable [5, 9].

This "critical aspect ratio" is theoretically a function of temperature and particle size, so a range of values are possible [53]. Empirical results suggest this aspect ratio can be approximated as 13-18 in the Al-Cu alloy system [9, 10]. Preliminary calculations based on expressions given by Boyd *et al.* are consistent with this value, predicting that this critical aspect ratio is likely between 10 and 20 for temperatures and particle sizes of interest [53]. For simplicity, we choose a single value: 15. In other words, we assume that once the aspect ratio of a θ′ particle drops to 15 or below, it transforms into the θ phase. The θ phase forms as relatively large, globular particles, and is not an effective strengthening precipitate. Furthermore, due to their incoherent nature and high interfacial energy, θ particles tend to coarsen rapidly and consume nearby θ′ particles. Thus, the θ′ to θ phase transformation corresponds to a dramatic loss in mechanical properties for the alloy [3, 4, 14, 15].

Given these considerations, the point at which the aspect ratio of one or more simulated θ′ particles reduces to 15 is assumed to be the "onset of instability" in the virtual microstructure, and the physical time (t) when this onset occurs in the simulation is termed the "duration of stability" for the simulated alloy. The duration of stability was determined for each simulated alloy at each temperature. If the end of the 200-hour simulation was reached without the onset of instability, the simulated alloy was considered thermally stable at that temperature. It is noted that recent studies of coarsening in Ni alloys have also used aspect ratio to quantify microstructural evolution [54]. By using the critical aspect ratio metric as a proxy for θ′ to θ transformation in the virtual microstructure, we increased the computational efficiency of our simulations compared to a direct simulation of the phase transformation. As described later, we also found that this criterion yielded realistic predictions.

2.5. Microstructural Characterization

The microstructural evolution predicted by phase field simulations was compared to the evolution of experimental microstructures. Specifically, as-aged samples of 319 (a conventional θ′ strengthened Al alloy) and RR350 (a θ′ strengthened Al alloy containing Mn and Zr with improved thermal stability [6]) were held at elevated temperatures (one sample each at 200 °C and 300 °C) for 200 hours and then air cooled (composition and aging conditions described elsewhere [14]). After polishing and etching with Keller's reagent (by volume: 95% H_2O, 2.5% HNO_3, 1.5% HCl, 1% HF) the samples were examined using a Hitachi S4800 Field Emission Gun - Scanning Electron Microscope (FEG-SEM) in secondary electron (SE) mode.

As-aged RR350 and 319 were also examined using HAADF scanning transmission electron microscopy. Thin-foil specimens of each alloy were prepared for high-resolution electron microscopy using standard methods of electropolishing, where 3-mm diameter x 100-μm thick discs were electropolished with a TenuPol system, as described in more detail elsewhere [3]. A JEOL 2200FS STEM/TEM instrument equipped with a CEOS GmbH corrector for the illuminating lenses allowed acquisition of HAADF images of electron-transparent alloy grains oriented via a double-tilt specimen holder with the electron beam incident along a matrix <001> zone-axis orientation. Details for acquisition of the HAADF images are given elsewhere [3]. The disc-shaped θ′ precipitates are seen edge-on in bright contrast with HAADF imaging of this zone orientation, as seen in Figure 4a.

3. Results and Discussion

In Section 2, we introduced the phase-field model, and the generation of the initial microstructure. In Section 3.1 below, we examine how the simulated microstructures evolve, particularly the distribution of aspect ratios. Based upon our assumption (Section 2.4 above) that once precipitates drop below a critical aspect ratio, they will rapidly transform into the equilibrium θ phase, we construct "stability maps" in Section 3.2, showing how reductions of Cu mobility and interfacial free energy affect the time required for the onset of θ′ to θ phase transformation at elevated temperatures. Section 3.3 compares the phase-field results to previous models and to experimental results. Finally, in section 3.4, we discuss the results specifically in comparison to specific alloys where microalloying may affect both interfacial energies and diffusion between the matrix and θ′ phase.

3.1. *Evolution of θ′ Aspect Ratio*

In general, the phase field simulations predicted that larger particles grew at the expense of smaller particles and all particles underwent thickening and shortening as they approached the equilibrium aspect ratio. Figure 5 gives a summary of this microstructural evolution, specifically for the baseline simulated alloy at 300 ^{o}C. The largest and smallest θ′ particles in the simulation are highlighted, and their evolution can be seen by comparing Figure 5a (the beginning of the simulation) to 5b (after 100 hours). While not visually dramatic, the smaller particle has shrunk while the larger particle has grown and both have reduced in aspect ratio, as is expected during overaging. A clearer demonstration of the coarsening tendency is shown in a map of Cu's chemical potential in the evolving microstructure at 300 ^{o}C (Figure 5c). Here, it is obvious that Cu has the highest potential at the semicoherent interface of particles, and will thus tend to migrate to where chemical potential is lowest, coherent interfaces and larger particles. There is also substantial interaction of the stress fields around precipitates, as shown in Figure 5d. Note that dislocations were not explicitly accounted for in these simulations. It has been shown that dislocations in the α-Al matrix play a significant role in the nucleation and growth of θ′ particles [47]. In a physical microstructure, it is possible that dislocations may accommodate some amount of the inter-particle strain predicted by phase field simulations [5].

[Figure 5 about here]

The distribution of particle aspect ratios over time was tracked in each simulated alloy at each temperature to determine when the minimum aspect ratio reduced to the critical value of 15 (chosen to represent the "duration of stability" as discussed in section 2.3). We then examine this evolution as a function of interfacial energy and Cu diffusivity. Figure 6 illustrates the effects of thermodynamic and kinetic stabilization on the rate of microstructural degradation in Al-Cu alloys at 400 °C. With no stabilization, the lower aspect ratio particles (which are also the smallest particles) undergo immediate and rapid shape evolution. With intermediate kinetic and thermodynamic stabilization, the minimum θ′ aspect ratio is relatively unchanged until approximately 90 hours into the simulation (possibly an effect of time-dependent impingement of Cu diffusion fields). After 90 hours, the minimum aspect ratio decreases monotonically and reaches the critical value of 15 before the end of the simulation. When the microstructure is fully stabilized, it retains its as-aged morphology and little evolution is observed during the simulation. The duration of stability of each simulated alloy at each temperature provides a single data point, and when collected, these data points provide insight into the overall trends of microstructural stability versus temperature and alloy modification. This analysis is described in the following section.

[Figure 6 about here]

3.2. *Stability Maps for θ′ to θ Evolution up to 400 °C*

The duration of stability described in Section 2.3 is plotted as a function of temperature for each simulated alloy in Figure 7. Each alloy is represented by a black dot, located on the plot according to its extent of kinetic ($Q_{diff,Cu}$) and thermodynamic ($\gamma_{semi\text{-}coherent}$, denoted "interfacial energy") modification relative to a baseline Al-Cu alloy. Interpolation between data points is done using a modified Shepard's method [55]. If a simulated alloy reached the end of the 200 hour simulation without any particles attaining an aspect ratio of 15 or less, it is considered "thermally stable" and is indicated with dark blue shading.

[Figure 7 about here]

At 100 °C, all simulated alloys reach 200 hours without any θ′ particles attaining the critical aspect ratio of 15. Therefore, the "Regime of Stability" as annotated in Figure 7a includes all simulated alloys. In other words, no modifications to a binary Al-Cu alloy (represented by 0% interfacial energy modification and 0% $Q_{diff,Cu}$ modification) are necessary to achieve thermal stability at 100 °C. At 200 °C, the unmodified Al-Cu simulated alloy begins to show microstructural transformation before 200 hours.

At 300 °C, distinct regimes of stability and instability emerge. At this temperature, the unmodified simulated alloy is thermally destabilized early in the simulation. Furthermore, the thermal stability of any simulated alloy is most sensitive to the activation energy for Cu diffusion in that alloy (i.e. kinetics), and a 10 % modification to $Q_{diff,Cu}$ is sufficient to stabilize the simulated alloy. This observation suggests that a kinetic stabilization mechanism might be the most effective strategy to achieve microstructural stability at 300 °C. Considering ACMZ alloys, which experimentally demonstrate this level of thermal stability, it is likely that a mechanism which alters the kinetics of diffusion/coarsening/ledge growth would be adequate to account for such stability through solute segregation.

At 400 °C, the regime of instability has expanded significantly, indicating that a much greater modification to a baseline Al-Cu alloy is necessary to achieve thermal stability at this temperature. In contrast to the duration of stability map at 300 °C, these higher temperature results indicate that microstructural stability at 400 °C is sensitive to thermodynamic modifications and kinetic modifications to a similar degree.

3.3. *Comparison to Prior Analysis and Experiment*

In order to assess the quantitative accuracies and shortcomings of the present model, three key results are compared against prior analyses and experiments: θ′ diameter evolution, θ′ aspect ratio evolution, and the onset of θ formation as a function of time and temperature. Experimental results are compared with the baseline, unmodified simulated alloy (Figures 8 and 9), and an analytical model for θ′ aspect ratio evolution from the literature [56] is used in Figure 10 to generate duration of stability maps analogous to those shown in Figure 7.

[Figure 8 about here]

Although a direct comparison at a single temperature was not available, there is close agreement on the normalized mean θ′ diameter evolution between the phase field simulations of an unmodified, baseline Al-Cu alloy microstructure and prior experimental observations [57] as shown in Figure 8a. In a comparison with another prior work [9], mean aspect ratio had a similar initial condition and reduced over time during preconditioning in both simulation and experiment (note that the evolution of the minimum aspect ratio was used to generate the duration of stability maps in Figure 7, not the evolution of the mean aspect ratio). Experimentally, the aspect ratio dropped quickly within the first several hours of preconditioning, with the rate of change gradually reducing thereafter. The phase field simulations also predicted a rapid initial drop in mean aspect ratio, followed by a more consistent rate of change, a rate which approximately matches the later stages of the experimental preconditioning.

Both the aspect ratio and diameter evolutions were evaluated in a heated TEM foil, which may have resulted in surface diffusion of Cu and accelerated microstructural evolution [11, 19]. In addition, there are well documented difficulties in accurately measuring the thickness of disc-shaped θ′ particles, with low magnification measurements generally overestimating average thickness by a factor of ~2 [2, 52]. This would artificially depress the calculated aspect ratio and may be partially responsible for the discrepancy seen in Figure 8b.

We now compare the phase field prediction of θ′ to θ transformation to experimental observations in existing literature. Consistent with the phase field simulations, this transformation is observed in Al-Cu alloys when held at temperatures of 200 ^{o}C and above for adequate time. Some experiments in this area [9, 53, 57-60] have been either isothermal or isochronal studies, allowing the combination of temperature and time leading to θ formation to be pinpointed. Results from these studies are plotted on a semi-log chart in Figure 9, along with predictions of the same from the current phase field simulations of the baseline alloy. There is reasonable agreement between phase field predictions and experiment, suggesting that the method used to predict θ′ to θ transformation in this work is adequately predictive. This comparison is an important benchmark for the phase field model used in this study. Given that a two dimensional simulation is used to predict the evolution of a three dimensional system, inaccuracies such as reduced lengths of diffusion paths and uncertainty in particle cross-section were introduced. These are in addition to the inherent limitations of the phase field model, such as the use of imprecise input parameters meant to represent complex, temperature-dependent processes and difficulty capturing important atomic-scale phenomena like ledge nucleation. Therefore, the fact that both prior work and the present simulations suggest relatively consistent times required for θ′ to θ transformation in binary Al-Cu alloys is key to establishing the usefulness of the model's other results. And while the use of two dimensional simulations rather than three dimensional simulations represents a tradeoff between the number of simulations which can be performed and their individual accuracy, this indicates that the penalty to accuracy was not severe.

[Figure 9 about here]

Along with developing phase field simulations which are representative of binary Al-Cu alloys, one key objective of the present work is to quantify the thermodynamic and/or kinetic modifications necessary to stabilize the Al-Cu microstructure at different temperatures. This result is captured in the duration of stability maps, shown in Figure 7. Given that these predictions involve adjusting parameters that cannot be directly controlled in alloy design, they cannot be directly compared to experimental results. Instead we compare the predictions to an analytical model for θ′ aspect ratio evolution that explicitly accounts for semi-coherent interfacial energy and the diffusivity of Cu [56]. Specifically, the model predicts aspect ratio evolution of a single particle in an equilibrium solid solution. This model is captured in three equations. The first, Equation 11, states that the aspect ratio of a θ′ will evolve over time, at a rate which depends on the thermodynamic driving force for the evolution (captured in the ϕ term), and the limiting kinetics of the system (captured in the β term). Equation 12 describes how the kinetic β term depends on alloy chemistry, temperature, copper diffusivity, and ledge growth. Equation 13 describes how the thermodynamic ϕ term depends on the value of the particle's instantaneous aspect ratio in relationship to the equilibrium aspect ratio. The definition and values of each parameter used in these equations is given in Table 6.

$$\beta t = \phi(AR) - \phi(AR_o) \tag{11}$$

$$\beta = \frac{1}{3}\left(\frac{\pi}{4V}\right)^{\frac{2}{3}}\left(\frac{6V_m x_{Cu,\alpha}}{RT}\right)\left(\frac{D_{Cu}}{\alpha\lambda}\right)\left(\frac{\gamma_{semicoherent}}{x_{Cu,\theta'} - x_{Cu,\alpha}}\right) \tag{12}$$

$$\begin{aligned}\phi(AR) = {} & \frac{1}{AR^{\frac{1}{3}}\left(AR - AR_{eq}\right)} - \frac{AR^{\frac{1}{3}}}{AR_{eq}\left(AR - AR_{eq}\right)} + \frac{1}{2AR_{eq}^{\frac{5}{3}}}\left(\ln\left(\frac{\left(AR - AR_{eq}\right)^{\frac{1}{3}}}{AR^{\frac{1}{3}} - AR_{eq}^{\frac{1}{3}}}\right)\right) \\ & - \frac{1}{\sqrt{3}}\tan^{-1}\left(\frac{AR^{\frac{1}{3}}}{AR^{\frac{1}{3}} + 2AR_{eq}^{\frac{1}{3}}}\right)\end{aligned} \tag{13}$$

[Table 6 about here]

In the case of an as-aged θ′ particle with an aspect ratio much greater than the equilibrium value, this model predicts that the aspect ratio will approach the equilibrium value at a rate that decreases with time [56, 57]. To compare this model's predictions to those of the present phase field simulations, the parameters given in Table 6 were substituted into Eqs. 11 – 13 with systematic variations in $Q_{diff,Cu}$ and $\gamma_{semicoherent}$ (Section 2.2). The model was then used to calculate the preconditioning time required for the defined θ′ particle to reach an aspect ratio of 15, the same critical condition used for the phase field duration of stability maps. This allows for new duration of stability maps to be generated based entirely on the analytical model. These are shown for 300 ^{o}C and 400 ^{o}C in Figure 10 (the analytical model predicts that all alloy variations are stable at 100 ^{o}C and 200 ^{o}C).

[Figure 10 about here]

There are some similarities and some discrepancies between the two sets of duration of stability maps. Generally speaking, there is agreement on the effect of $Q_{diff,Cu}$ modification, whereas the phase field simulations are more sensitive to $\gamma_{semi-coherent}$ modification (especially at 400 ^{o}C). According to the analytical model, $Q_{diff,Cu}$ is the dominant parameter controlling microstructural stability at every temperature. The increased sensitivity to $\gamma_{semicoherent}$ modification in the phase field simulations may be partly due to the curvature of the semi-coherent interface, which is assumed to be flat in the analytical model. This curvature increases the total area of the semi-coherent interface, and therefore its contribution to the system's total free energy. The analytical model also does not account for a particle's growth or shrinking during coarsening nor the nature of the surrounding particles – their number density, aspect ratio distribution, non-uniform Cu content due to dissolving particles *etc*. There are likely important interactive effects between particles that are not captured by the analytical model. Additionally, note that Eq.s 11-13 (as well as the Langer-Schwartz-Wagner coarsening model modified to describe disc-shaped particles [53]) predict that the rates of shape evolution and coarsening are equally sensitive to D_{Cu} and $\gamma_{semi-coherent}$: Eq. 12 indicates a dependence on the product $(D_{Cu})(\gamma_{semicoherent})$, suggesting that these cannot be entirely decoupled. However, in our calculations, D_{Cu} is being modified exponentially by adjustments in $Q_{diff,Cu}$ while

$\gamma_{semi-coherent}$ is being varied linearly, thus explaining the sensitivity to $Q_{diff,Cu}$ shown in Fig. 10. This was done to reflect key physical aspects of θ′ evolution and potential stabilization mechanisms, as described in Section 2.2.

Overall, this comparison reveals the contrasting nature of the analytical and phase field approaches to predicting θ′ aspect ratio evolution. While the analytical approach invokes simplified particle geometry and surroundings, it also addresses a gap in the phase field approach: it allows for precise and direct modifications to particle descriptors such as interfacial energy, which require multiple fitting parameters in phase field. Moving forward, a more mechanistic phase field simulation that can explicitly illustrate the effects of solute segregation (including not only interfacial energy and Cu mobility reduction, but also solute drag and strain field interactions) is in order. The following section discusses the implications of the present phase field simulation results for understanding current alloys and designing improved alloys.

3.4. *Relating Phase Field Predictions to Conventional and ACMZ Alloys*

The trends in duration of stability shown in Figure 7 correspond well with experimental observations [6]. The microstructural evolution that occurs during 300 °C preconditioning in θ′ strengthened cast aluminum alloys 319 and RR350 is shown in Figure 11, for comparison with phase field results. In agreement with experiment [9], all simulated alloys in the phase field simulations are thermally stable at 100 °C, even the unmodified, baseline Al-Cu alloy. At 200 °C, the unmodified virtual Al-Cu alloy is destabilized near the end of the 200 hour test. The microstructure of conventional alloys (such as 319) held at this temperature, demonstrate moderate to severe coarsening of θ′ particles, and sometimes θ′ to θ transformation, depending on alloying and the duration of exposure [3, 14].

[Figure 11 about here]

At 300 °C, the distinct regimes of stability and instability predicted by simulations correspond to the divergence in microstructure and mechanical properties between conventional and thermally stable alloys. Thermally stable ACMZ alloys such as RR350 largely retain their as-aged microstructures at this temperature while conventional alloys such as 319 show extensive degradation of their as-aged microstructures at this temperature [2-4, 6-8]. While the precise extent of thermodynamic and/or kinetic modification caused by the segregation of Mn and Zr to the interface of θ′ particles in RR350 is unknown, the observations shown in Figure 11 can be generally related to the stability map shown in Figure 7c. If the model parameters could be used to accurately capture the nature of θ′ interfacial energy and Cu diffusivity in 319, it would be expected to correspond to a simulated alloy in the regime of instability shown in the bottom of Figure 7c. A simulated alloy which recreates RR350, meanwhile, would be located somewhere in the regime of stability in Figure 7c, as it is thermally stable at 300 °C. At 400 °C, however, RR350 precipitates are not thermally stable [6], so the simulated alloy recreating RR350 must also be located outside the regime of stability shown in Figure 7d.

The discussion above highlights the challenge of designing a θ′ strengthened aluminum alloy that is thermally stable at 400 °C. At the time of this study, no precipitate strengthened Al-Cu alloy has demonstrated extended microstructural stability at this temperature. Referring to Figure 7, the regime of stability at 400 °C is much more limited than at 300 °C, and appears to exclude even novel alloys with improved thermal stability [6]. Present results suggest that new alloy design strategies will be necessary to address this challenge. While a kinetic stabilization mechanism such as solute drag or a diffusion barrier at the θ′ interface might be adequate to produce the 300 °C capable alloys that have been observed [6], the introduction of a synergistic thermodynamic mechanism which can effectively reduce interfacial energy will likely be necessary to stabilize the Al-Cu microstructure at 400 °C.

In addition to providing insight into how solute segregation driven thermal stabilization mechanisms might operate in the Al-Cu system, these results indicate the importance of kinetic considerations in phase field modeling of the Al-Cu system. Generally speaking, the aspect ratio of θ′ particles increases during aging as radial growth outpaces particle thickening, reaches a maximum in the as-aged state, and then decreases as particles continue to thicken without mean diameter growth in the process of coarsening [46, 67]. Experimental observations suggest that, with the exception of very small particles, θ′ evolves into θ before it attains the equilibrium aspect ratio (reported as 2-5) [1, 28, 30, 33, 67, 68]. Thus, thermodynamic equilibrium conditions do not offer a complete description of microstructural evolution and the ability to quantify particle coarsening kinetics enhances the utility of present generation phase field models for the Al-Cu system.

4. Conclusions

The thermal stability of the α/θ′ microstructure in Al-Cu alloys was studied using a combination of phase field simulations and experimental observations. Simulations were carried out using the MOOSE phase field module, and experimental observations were made by exposing two different θ′ strengthened alloys to elevated temperatures for 200 hours. In agreement with the experimental results, the phase field simulations predicted that strengthening θ′ precipitates are relatively stable at temperatures of 200 °C and below in unmodified Al-Cu alloys. At 300 °C and above, the α/θ′ microstructure is thermally destabilized, and rapid θ′

coarsening and shape evolution take place.

The rate of shape evolution predicted by phase field simulations was similar to that observed experimentally. In order to predict the onset of detrimental θ′ to θ transformation, a critical θ′ aspect ratio criterion was proposed. Using this criterion, the phase field simulations accurately predicted the time required for the onset of θ formation in a binary Al-Cu alloy as a function of temperature. The phase field simulations also predicted that thermodynamic and/or kinetic modifications to a simulated alloy can lead to microstructural stability at higher temperatures.

The mobility of Cu in the α/θ′ microstructure was shown to be the dominant factor in determining its morphological stability at 300 °C. Phase field simulations predict that a reduction in effective Cu diffusivity is adequate to thermally stabilize the α/θ′ microstructure at this temperature. At 400 °C, however, significant modification to both Cu mobility and interfacial energy of θ′ particles is required to effectively stabilize the microstructure. These predictions help explain the thermal stability of recently reported Al-Cu-Mn-Zr alloys, whose as-aged microstructure is coarsening resistant at 300 °C but undergoes substantial degradation at 400 °C.

Finally, these 300 °C and 400 °C phase field predictions were compared to predictions made by an analytical model for θ′ aspect ratio evolution reported previously. The analytical model agreed on the effect of reducing effective Cu diffusivity, but was much less sensitive to interfacial energy reduction compared to the phase field simulations. This discrepancy suggests that geometric effects such as particle curvature and particle volume change, as well as interactive effects between growing and shrinking particles that occur during coarsening, influence θ′ precipitate shape evolution. Such effects are difficult to capture in an analytical model of a single particle but can be evaluated using phase field simulations.

Acknowledgements

Research sponsored by the Laboratory Directed Research and Development Program of Oak Ridge National Laboratory, managed by UT-Battelle, LLC. Early research also sponsored by the U.S. Department of Energy, Assistant Secretary for Energy Efficiency and Renewable Energy, Office of Vehicle Technologies, as part of the Propulsion Materials Program. PS was supported by the Department of Defense (DoD) through the National Defense Science & Engineering Graduate Fellowship (NDSEG) Program. JRM is supported by the USDOE Office of Science, Basic Energy Sciences, Materials Science and Engineering Division. This research used resources of the Oak Ridge Leadership Computing Facility at the Oak Ridge National Laboratory, which is supported by the Office of Science of the U.S. Department of Energy under Contract No. DE- AC05-00OR22725. The authors would also like to thank Sarma Gorti and German Samolyuk for their technical review. Declaration of interest – None.

References

[1] M.A. Meyers, K.K. Chawla, Mechanical Behavior of Materials, Cambridge University Press, 2009.

[2] S. Roy, L.F. Allard, A. Rodriguez, T.R. Watkins, A. Shyam, Comparative Evaluation of Cast Aluminum Alloys for Automotive Cylinder Heads: Part I—Microstructure Evolution, Metall and Mat Trans A 48(5) (2017) 2529-2542.

[3] S. Roy, L.F. Allard, A. Rodriguez, W.D. Porter, A. Shyam, Comparative Evaluation of Cast Aluminum Alloys for Automotive Cylinder Heads: Part II—Mechanical and Thermal Properties, Metall and Mat Trans A 48(5) (2017) 2543-2562.

[4] Aluminum and Aluminum Alloys ASM Specialty Handbook, ASM International, Materials Park, OH, 2010.

[5] Porter, Easterling, Phase Transformations in Metals and Alloys, Permagon Press1981.

[6] A. Shyam, S. Roy, D. Shin, L. Allard, Y. Yamamoto, J. Morris, B. Mazumder, A. Rodriguez, T. Watkins, J. Haynes, Cast Aluminum Alloys with Extreme Resistance to Coarsening, In Review (2018).

[7] H. Sehitoglu, T. Smith, X. Qing, H. Maier, J.A. Allison, Stress-strain response of a cast 319-T6 aluminum under thermomechanical loading, Metall and Mat Trans A 31(1) (2000) 139-151.

[8] E. Rincon, H.F. Lopez, M.M. Cisneros, H. Mancha, Temperature effects on the tensile properties of cast and heat treated aluminum alloy A319, Materials Science and Engineering: A 519(1–2) (2009) 128-140.

[9] P. Merle, F. Fouquet, Coarsening of θ′ plates in al-cu alloys—I. experimental determination of mechanisms, Acta Metallurgica 29(12) (1981) 1919-1927.

[10] Z. Gao, X. Zhang, M.a. Chen, Influence of strain rate on the precipitate microstructure in impacted aluminum alloy, Scripta Materialia 59(9) (2008) 983-986.

[11] C. Laird, H. Aaronson, Mechanisms of formation of θ and dissolution of θ′ precipitates in an Al-4% Cu alloy, Acta Metallurgica 14(2) (1966) 171-185.

[12] J.F. Nie, B.C. Muddle, Microstructural design of high-strength aluminum alloys, Journal of Phase Equilibria 19(6) (1998) 543.

[13] V. Kokotin, U. Hecht, Molecular dynamics simulations of Al–Al 2 Cu phase boundaries, Computational Materials Science 86 (2014) 30-37.

[14] P. Shower, S. Roy, C.S. Hawkins, A. Shyam, The effects of microstructural stability on the compressive response of two cast aluminum alloys up to 300°C, Materials Science and Engineering: A 700 (2017) 519-529.

[15] B. Milligan, A. Shyam, C. Hawkins, S. Roy, The effect of microstructural stability on the creep behavior of cast Al-Cu alloys at 300°C, In Review (2016).
[16] M. Javidani, D. Larouche, Application of cast Al–Si alloys in internal combustion engine components, International Materials Reviews 59(3) (2014) 132-158.
[17] D. Shin, A. Shyam, S. Lee, Y. Yamamoto, J.A. Haynes, Solute segregation at the Al/θ′-Al_2Cu interface in Al-Cu alloys, Acta Materialia 141 (2017) 327-340.
[18] C. Monachon, M.E. Krug, D.N. Seidman, D.C. Dunand, Chemistry and structure of core/double-shell nanoscale precipitates in Al–6.5Li–0.07Sc–0.02Yb (at.%), Acta Materialia 59(9) (2011) 3398-3409.
[19] R. Sankaran, C. Laird, Kinetics of growth of platelike precipitates, Acta Metallurgica 22(8) (1974) 957-969.
[20] L.-Q. Chen, Phase-field models for microstructure evolution, Annual review of materials research 32(1) (2002) 113-140.
[21] W.J. Boettinger, J.A. Warren, C. Beckermann, A. Karma, Phase-field simulation of solidification, Annual review of materials research 32(1) (2002) 163-194.
[22] M. Mamivand, M.A. Zaeem, H. El Kadiri, A review on phase field modeling of martensitic phase transformation, Computational Materials Science 77 (2013) 304-311.
[23] I. Steinbach, Phase-field models in materials science, Modelling and simulation in materials science and engineering 17(7) (2009) 073001.
[24] Y. Wang, J. Li, Phase field modeling of defects and deformation, Acta Materialia 58(4) (2010) 1212-1235.
[25] J. Wang, C. Wolverton, S. Müller, Z.-K. Liu, L.-Q. Chen, First-principles growth kinetics and morphological evolution of Cu nanoscale particles in Al, Acta Materialia 53(9) (2005) 2759-2764.
[26] V. Fallah, J. Stolle, N. Ofori-Opoku, S. Esmaeili, N. Provatas, Phase-field crystal modeling of early stage clustering and precipitation in metal alloys, Physical Review B 86(13) (2012) 134112.
[27] V. Fallah, N. Ofori-Opoku, J. Stolle, N. Provatas, S. Esmaeili, Simulation of early-stage clustering in ternary metal alloys using the phase-field crystal method, Acta Materialia 61(10) (2013) 3653-3666.
[28] H. Liu, J. Nie, Phase field simulation of microstructures of Mg and Al alloys, Materials Science and Technology (2017) 1-14.
[29] H. Liu, B. Bellón, J. Llorca, Multiscale modelling of the morphology and spatial distribution of θ′ precipitates in Al-Cu alloys, Acta Materialia 132 (2017) 611-626.
[30] D.Y. Li, L.Q. Chen, Computer simulation of stress-oriented nucleation and growth of θ′ precipitates inAl–Cu alloys, Acta Materialia 46(8) (1998) 2573-2585.
[31] Y. Ji, B. Ghaffari, M. Li, L.-Q. Chen, Phase-field modeling of θ′ precipitation kinetics in 319 aluminum alloys, Computational Materials Science 151 (2018) 84-94.
[32] K. Kim, A. Roy, M. Gururajan, C. Wolverton, P. Voorhees, First-principles/Phase-field modeling of θ′ precipitation in Al-Cu alloys, Acta Materialia 140 (2017) 344-354.
[33] S.Y. Hu, J. Murray, H. Weiland, Z.K. Liu, L.Q. Chen, Thermodynamic description and growth kinetics of stoichiometric precipitates in the phase-field approach, Calphad 31(2) (2007) 303-312.
[34] L. Chen, C. Wolverton, V. Vaithyanathan, Z. Liu, Modeling solid-state phase transformations and microstructure evolution, Mrs Bulletin 26(03) (2001) 197-202.

[35] V. Vaithyanathan, C. Wolverton, L.Q. Chen, Multiscale modeling of θ′ precipitation in Al–Cu binary alloys, Acta Materialia 52(10) (2004) 2973-2987.
[36] M.R. Tonks, D. Gaston, P.C. Millett, D. Andrs, P. Talbot, An object-oriented finite element framework for multiphysics phase field simulations, Computational Materials Science 51(1) (2012) 20-29.
[37] S.Y. Hu, M.I. Baskes, M. Stan, L.Q. Chen, Atomistic calculations of interfacial energies, nucleus shape and size of θ′ precipitates in Al–Cu alloys, Acta Materialia 54(18) (2006) 4699-4707.
[38] J.W. Cahn, J.E. Hilliard, Free Energy of a Nonuniform System. I. Interfacial Free Energy, The Journal of Chemical Physics 28(2) (1958) 258-267.
[39] A. Artemev, Y. Wang, A.G. Khachaturyan, Three-dimensional phase field model and simulation of martensitic transformation in multilayer systems under applied stresses, Acta Materialia 48(10) (2000) 2503-2518.
[40] M. Tonks, P. Millett, W. Cai, D. Wolf, Analysis of the elastic strain energy driving force for grain boundary migration using phase field simulation, Scripta Materialia 63(11) (2010) 1049-1052.
[41] M. Tonks, P. Millett, Phase field simulations of elastic deformation-driven grain growth in 2D copper polycrystals, Materials Science and Engineering: A 528(12) (2011) 4086-4091.
[42] F.R. Eshelman, J.F. Smith, Single-crystal elastic constants of Al_2Cu, Journal of Applied Physics 49(6) (1978) 3284-3288.
[43] D. Gerlich, E.S. Fisher, The high temperature elastic moduli of aluminum, Journal of Physics and Chemistry of Solids 30(5) (1969) 1197-1205.
[44] K. Kim, B.-C. Zhou, C. Wolverton, Interfacial stability of θ′/Al in Al-Cu alloys, Scripta Materialia 159 (2019) 99-103.
[45] Smithells Metals Reference Book, 7 ed., Butterworth-Heinemann, Oxford, 1992.
[46] D. Schwen, M. Tonks, Developing Phase Field Models. http://mooseframework.org/wiki/PhysicsModules/PhaseField/DevelopingModels, 2016).
[47] C. Liu, S.K. Malladi, Q. Xu, J. Chen, F.D. Tichelaar, X. Zhuge, H.W. Zandbergen, In-situ STEM imaging of growth and phase change of individual CuAlX precipitates in Al alloy, Scientific reports 7 (2017).
[48] Y. Li, G. Purdy, On the growth of Widmanstätten precipitates in an Al–Cu alloy, Acta Materialia 56(3) (2008) 364-368.
[49] G.R. Purdy, Edge-to-edge plane matching as a criterion for interphase boundaries of low energy, Metall and Mat Trans A 37(3) (2006) 857-863.
[50] L. Bourgeois, C. Dwyer, M. Weyland, J.-F. Nie, B.C. Muddle, The magic thicknesses of θ′ precipitates in Sn-microalloyed Al–Cu, Acta Materialia 60(2) (2012) 633-644.
[51] G. Purdy, J. Hirth, Transformation defects on θ′ precipitates in Al–Cu alloys, Philosophical magazine letters 86(03) (2006) 147-154.
[52] S.C. Weakley-Bollin, W. Donlon, W. Donlon, C. Wolverton, J.E. Allison, J.W. Jones, Modeling the age-hardening behavior of Al-Si-Cu alloys, Metall and Mat Trans A 35(8) (2004) 2407-2418.
[53] J.D. Boyd, R.B. Nicholson, The coarsening behaviour of θ″ and θ′ precipitates in two Al-Cu alloys, Acta Metallurgica 19(12) (1971) 1379-1391.
[54] L.T. Mushongera, M. Fleck, J. Kundin, Y. Wang, H. Emmerich, Effect of Re on directional -coarsening in commercial single crystal Ni-base superalloys: A phase field study, Acta Materialia 93 (2015) 60-72.

[55] D. Shepard, A two-dimensional interpolation function for irregularly-spaced data, Proceedings of the 1968 23rd ACM national conference, ACM, 1968, pp. 517-524.
[56] G. Shiflet, H. Aaronson, T. Courtney, Kinetics of the approach to equilibrium shape of a disc-shaped precipitate, Scripta Metallurgica 11(8) (1977) 677-680.
[57] P. Merle, J. Merlin, Coarsening of θ′ plates in Al-Cu alloys—II. influence of ledge mechanism, Acta Metallurgica 29(12) (1981) 1929-1938.
[58] F. Fouquet, P. Merle, M. Kohen, J. Merlin, P.F. Gobin, Variation du module d'young associee a la precipitation de la phase θ′ dans un alliage Al□Cu 4%, Acta Metallurgica 27(3) (1979) 315-326.
[59] J.M. Pelletier, G. Vigier, J. Merlin, P. Merle, F. Fouquet, R. Borrelly, Precipitation effects on thermopower in Al-Cu alloys, Acta Metallurgica 32(7) (1984) 1069-1078.
[60] J. Silcock, T. Heal, H. Hardy, Structural ageing characteristics of binary aluminium-copper alloys, J. Inst. Metals 82 (1954).
[61] S.K. Son, M. Takeda, M. Mitome, Y. Bando, T. Endo, Precipitation behavior of an Al–Cu alloy during isothermal aging at low temperatures, Materials Letters 59(6) (2005) 629-632.
[62] S.P. Ringer, W. Yeung, B.C. Muddle, I.J. Polmear, Precipitate stability in Al-Cu-Mg-Ag alloys aged at high temperatures, Acta Metallurgica et Materialia 42(5) (1994) 1715-1725.
[63] C. Laird, H.I. Aaronson, Mechanisms of formation of θ and dissolution of θ′ precipitates in an Al-4% Cu alloy, Acta Metallurgica 14(2) (1966) 171-185.
[64] C. Laird, R. Sankaran, The Structure Of Interphase Boundaries In Solids, Journal of Microscopy 116(1) (1979) 123-140.
[65] G. Thomas, M.J. Whelan, Observations of precipitation in thin foils of aluminium +4% copper alloy, The Philosophical Magazine: A Journal of Theoretical Experimental and Applied Physics 6(69) (1961) 1103-1114.

List of Figures

Figure 1 The free energy of formation of α and θ′ phases as a function of composition and temperature, as calculated by ThermoCalc. $f_{\alpha}(x_{Cu})$ and $f_{\theta'}(x_{Cu})$ in Equation 4 were derived using these data by a method described previously [35].

Figure 2 Bulk free energy functions of the α-Al and θ′ phases at 400 °C. Compare to Figure 1 in [32], Figure 11 in [35], and Figure 6 in [37].

Figure 3 A Wulff plot showing $\boldsymbol{\kappa_{\eta}}$ vs. interface orientation angle $\boldsymbol{\psi}$ as used in this study (Eq. 10). A $\boldsymbol{\kappa_{\eta}}$ vs. $\boldsymbol{\psi}$ relationship which has been used in prior studies is also plotted. The primary difference in the present study is the smoothing of the utilized energy minima.

Figure 4 The microstructure of an as-aged 319 aluminum alloy was used to create an initial microstructure for phase field simulations. (a) A representative micrograph of this as-aged microstructure and (b) the virtual microstructure used as the initial condition in the phase field simulations. (c) and (d) show histograms which compare the measured distribution to the simulated distribution of θ′ particle diameter and thickness, respectively.

Figure 5 A snapshot of microstructural evolution in a baseline Al-Cu alloy at 300 °C predicted by the phase field simulations. (a) The initial condition of the simulation, highlighting the area and aspect ratio of the largest and smallest particles and (b) the virtual microstructure after 100 hours of evolution, soon after the critical minimum aspect ratio of 15 was reached for the smallest particle with (c) and (d) being instantaneous maps of Cu chemical potential in the simulation and the stress field surrounding θ′ particles, respectively, after 100 hours of evolution at 300 °C.

Figure 6 Distribution of θ′ particle aspect ratio vs. time for selected simulated alloys at 400 °C. The baseline simulated alloy has no modifications. Its "duration of stability" at this temperature is 75 hours, at which time the lowest aspect ratio reaches a critical value of 15 (see Section 2.4). The "Partially Stabilized" simulated alloy has a 15% interfacial energy modification and 15% $Q_{\text{diff, Cu}}$ modification. Its "duration of stability" is 187 hours. The "Fully Stabilized" simulated alloy has 25% interfacial energy modification and 20% $Q_{\text{diff, Cu}}$ modification. Its minimum aspect ratio is greater than 15 for the duration of the simulation, so its "duration of stability" is considered 200 hours.

Figure 7 Duration of stability maps for 36 simulated alloys as a function of temperature. Each simulated alloy has a unique combination of thermodynamic modification (x-axis) and kinetic modification (y-axis) and is shown as a black dot. The regime of stability at each temperature is indicated with dark blue shading. (a) All simulated alloys are thermally stable at 100°C. (b) Slight kinetic or thermodynamic modification is needed to stabilize the simulated alloys at 200 °C. (c) A kinetic modification is needed to stabilize the simulated alloys at 300 °C. (d) Substantial modification to both thermodynamic and kinetic parameters is required to stabilize a simulated alloy at 400 °C.

Figure 8 Comparisons of phase field predictions and experimental observations for (a) mean θ′ diameter and (b) mean θ′ aspect ratio evolution over time. The mean diameter evolution was measured at 225 °C [57] and is compared to 300 °C baseline alloy phase field predictions, normalized to account for the fact that the initial condition in the experiment was a larger mean diameter than that used in the simulations. The mean aspect ratio evolution was measured at 275 °C [9] and is compared to 400 °C baseline phase field predictions, which matches it most closely.

Figure 9 Preconditioning time and temperature combinations for which θ′ to θ transformation occurs in binary Al-Cu alloys (all compositions in weight percent). Experimental observations [9, 53, 57-60] are plotted in black, fitted with a power law trend line. Predictions from the current phase field simulations are plotted in filled red squares and also fitted with a power law trend line. Some studies offered valuable information on θ′ to θ transformation, but either used differential scanning calorimetry [61] or could not be accurately plotted in this figure due to thin foil effects or wide time margins [62-65].

Figure 10 Duration of stability maps predicted by an analytical model for aspect ratio evolution [56] at (a) 300 ^{o}C and (b) 400 ^{o}C. The analogous duration of stability maps predicted by phase field simulations are shown in Figure 7.

Figure 11 The microstructural evolution that takes place in 319 (a conventional alloy) and RR350 (an alloy with improved thermal stability) when as-aged microstructures are held at 300 ^{o}C for 200 hours. 319 shows substantial coarsening of θ′ precipitates as well as phase transformation of θ′ into θ. Meanwhile, θ′ precipitates in RR350 retain their as-aged morphology at 300 ^{o}C. The as-aged micrographs were collected with HAADF, the preconditioned micrographs with SEM.

List of Tables

Table 1 Coefficients of the free energy functions used in this study for the solution and precipitate phases at each temperature. The form of these functions is given in Equation 6.

Table 2 Interfacial energies of the coherent and semi-coherent interfaces reported by Shyam *et al.* [6] were used to determine the gradient coefficient terms required by Eq. 7.

Table 3 Elastic Constants of Al and θ′, values from the literature [42, 43]

Table 4 Diffusional terms used in this study. The baseline activation energy value and the diffusional prefactor $D_o = 0.654 \left[\frac{cm^2}{sec}\right]$ \were taken from the literature [45], The formula used to find chemical mobility formula was taken from [35].

Table 5. Modifications to interfacial energy and gradient coefficients in the phase field simulations were introduced.

Table 6. Parameters used in the analytical model [56] for aspect ratio evolution of a single θ′ particle, defined by

Eq.s 11 – 13.

Figure 1

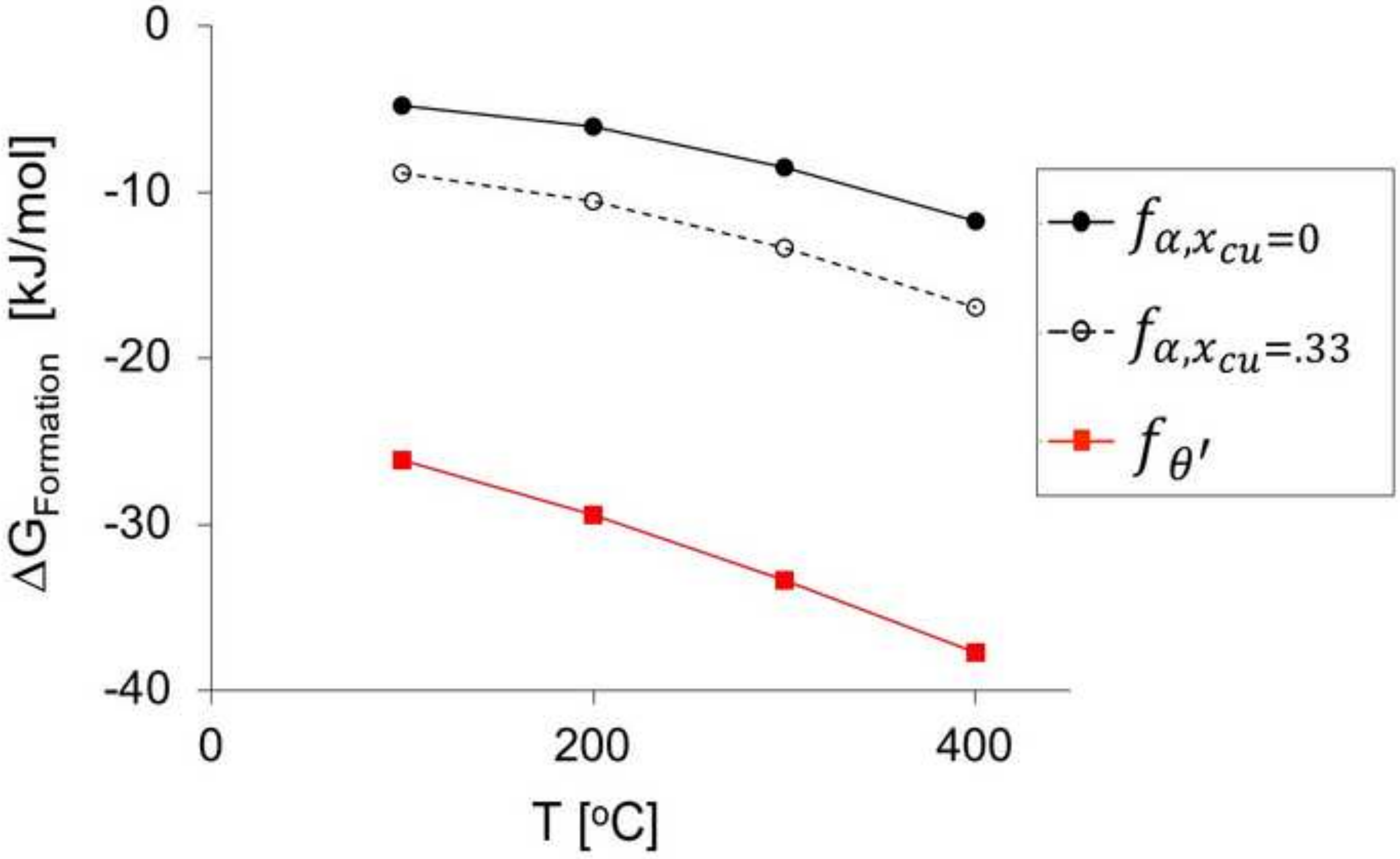

0
-10
-20
-30
-40
$\Delta G_{Formation}$ [kJ/mol]
0
200
400
T [^oC]
$f_{\alpha,x_{cu}=0}$
$f_{\alpha,x_{cu}=.33}$
$f_{\theta'}$

Figure 2

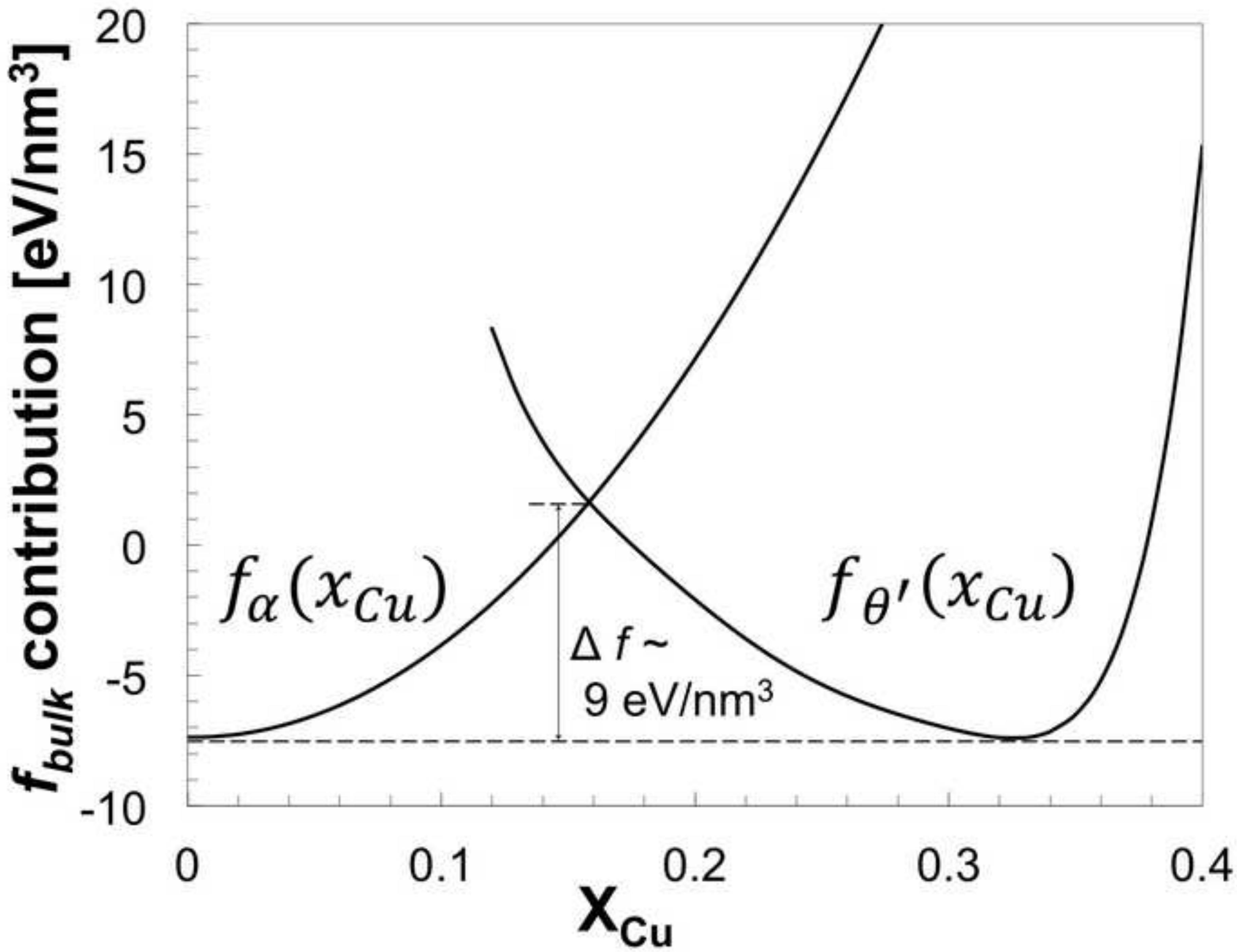

20
15
10
5
0
-5
-10
0
0.1
0.2
0.3
0.4
f_{bulk} contribution [eV/nm^3]
X_{Cu}
$f_\alpha(x_{Cu})$
$f_{\theta'}(x_{Cu})$
$\Delta f \sim$ 9 eV/nm^3

Figure 3

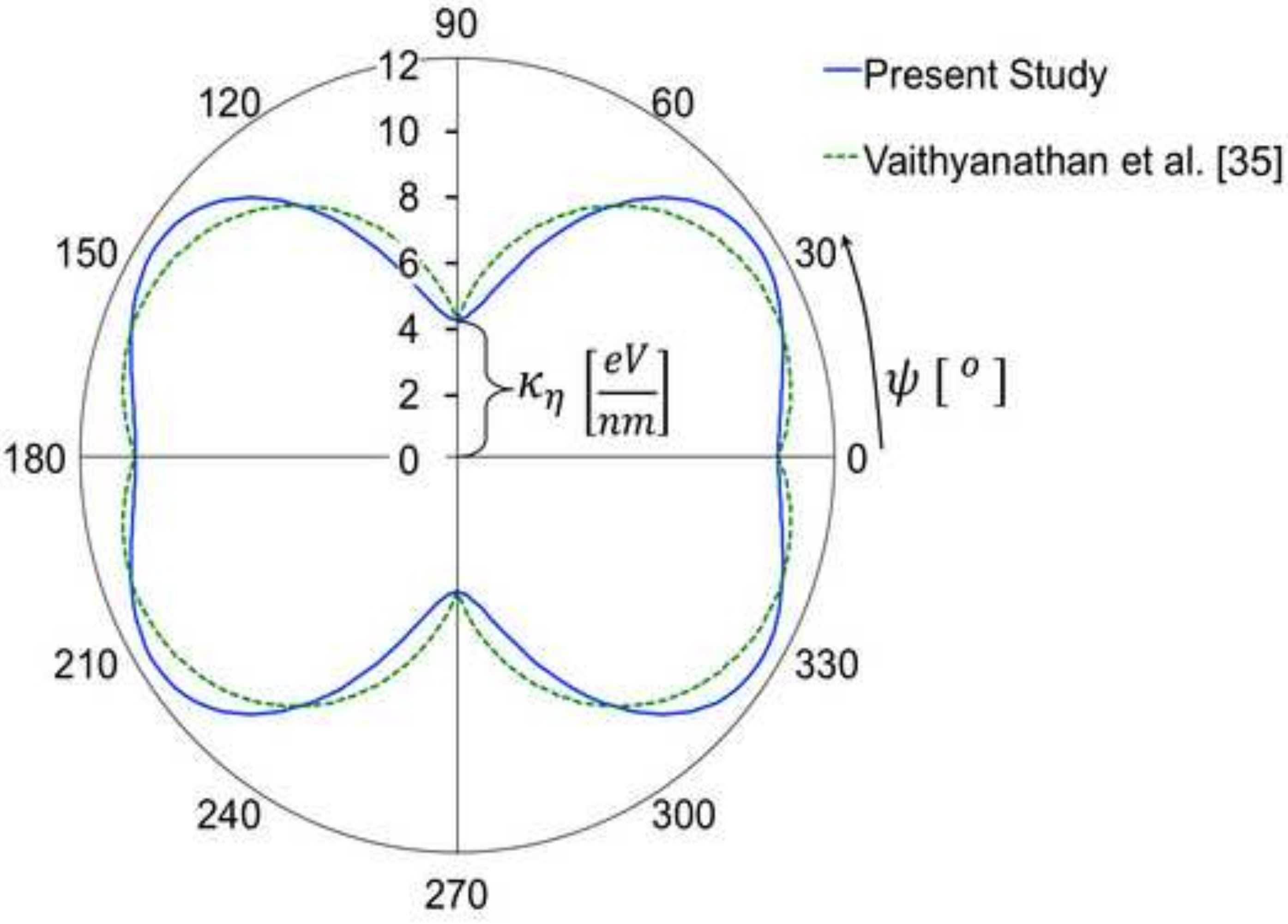
90
120
60
150
30
180
0
210
330
240
300
270
12
10
8
6
4
2
0
$\kappa_\eta \left[\frac{eV}{nm}\right]$
$\psi\ [\,^o\,]$
Present Study
Vaithyanathan et al. [35]

Figure 4

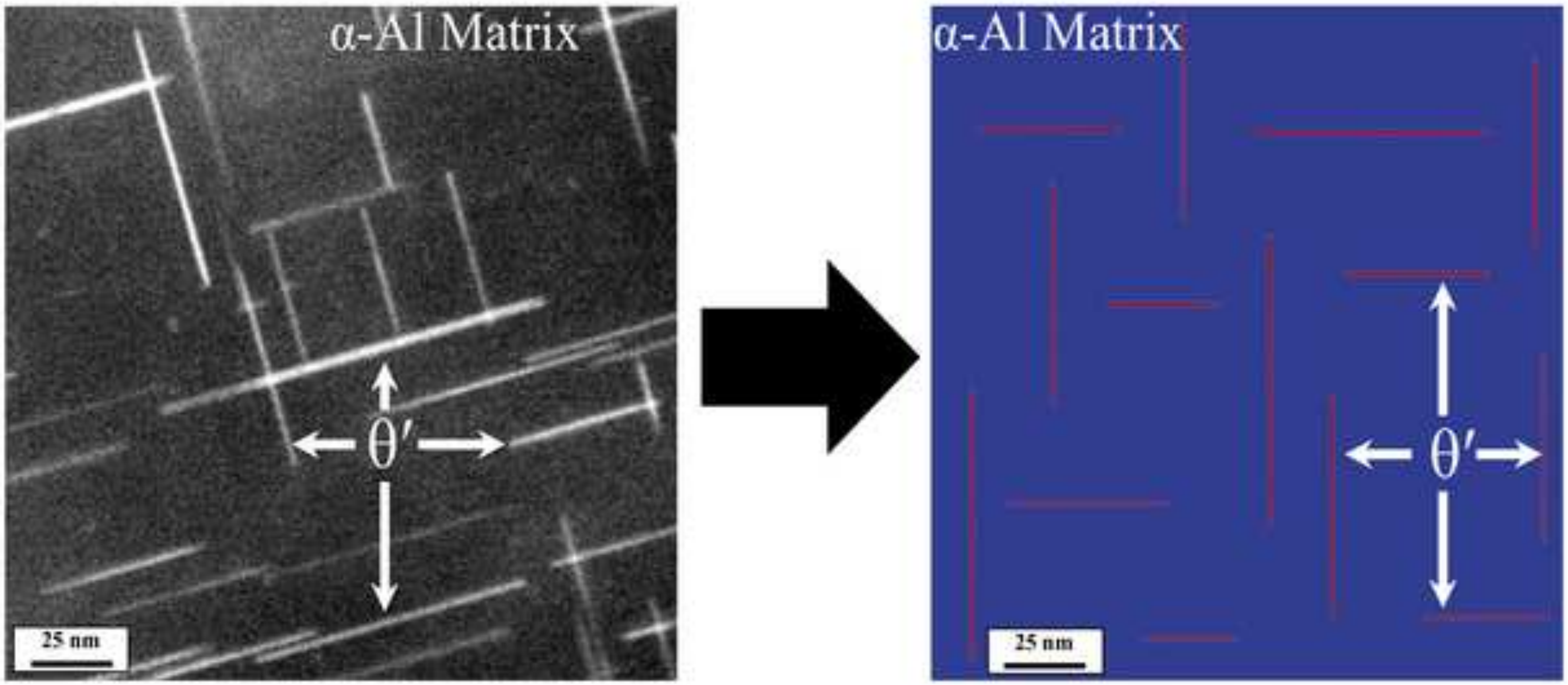

(a) As-aged 319 microstructure.

(b) Virtual microstructure used in simulations.

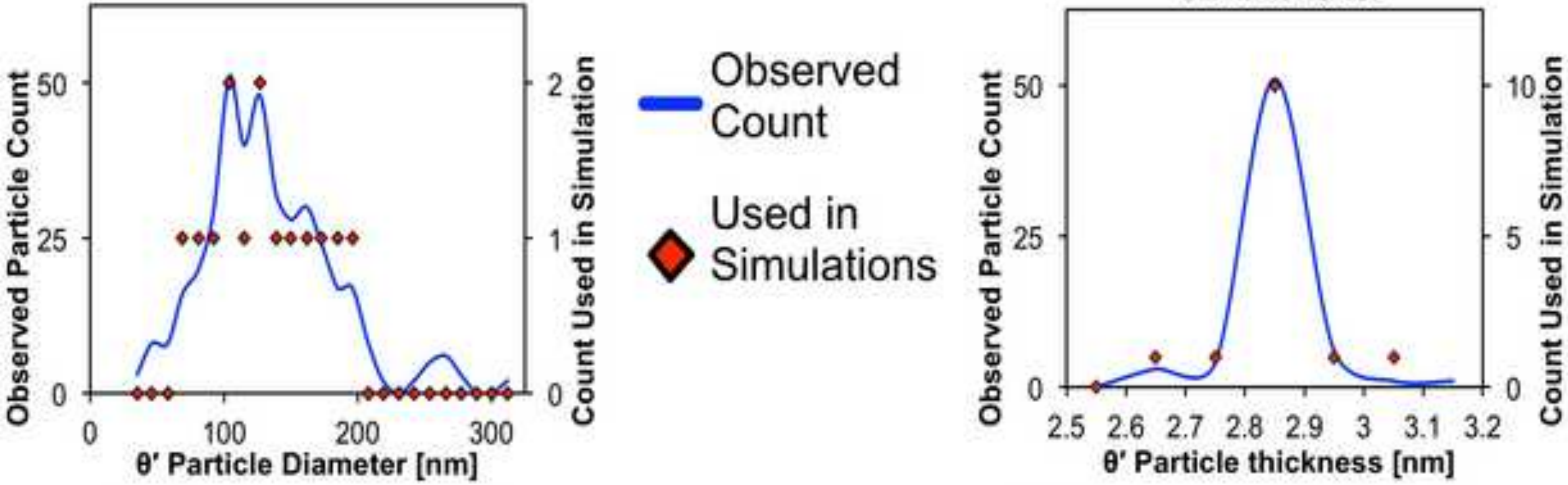

(c) Histogram of of θ′ diameter.

(d) Histogram of θ′ thickness.

Figure 5

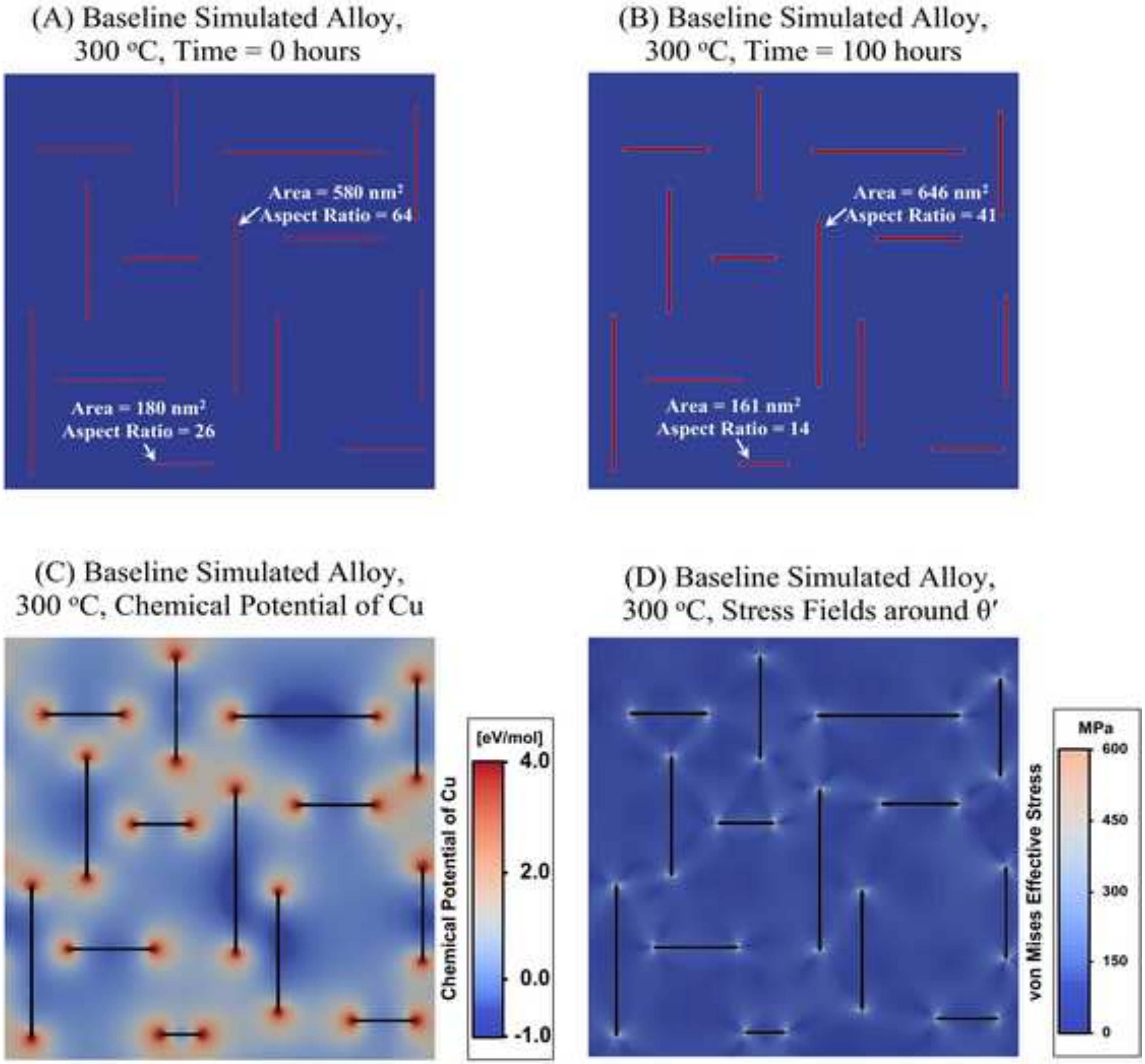
(A) Baseline Simulated Alloy, 300 °C, Time = 0 hours

(B) Baseline Simulated Alloy, 300 °C, Time = 100 hours

(C) Baseline Simulated Alloy, 300 °C, Chemical Potential of Cu

(D) Baseline Simulated Alloy, 300 °C, Stress Fields around θ′

Figure 6

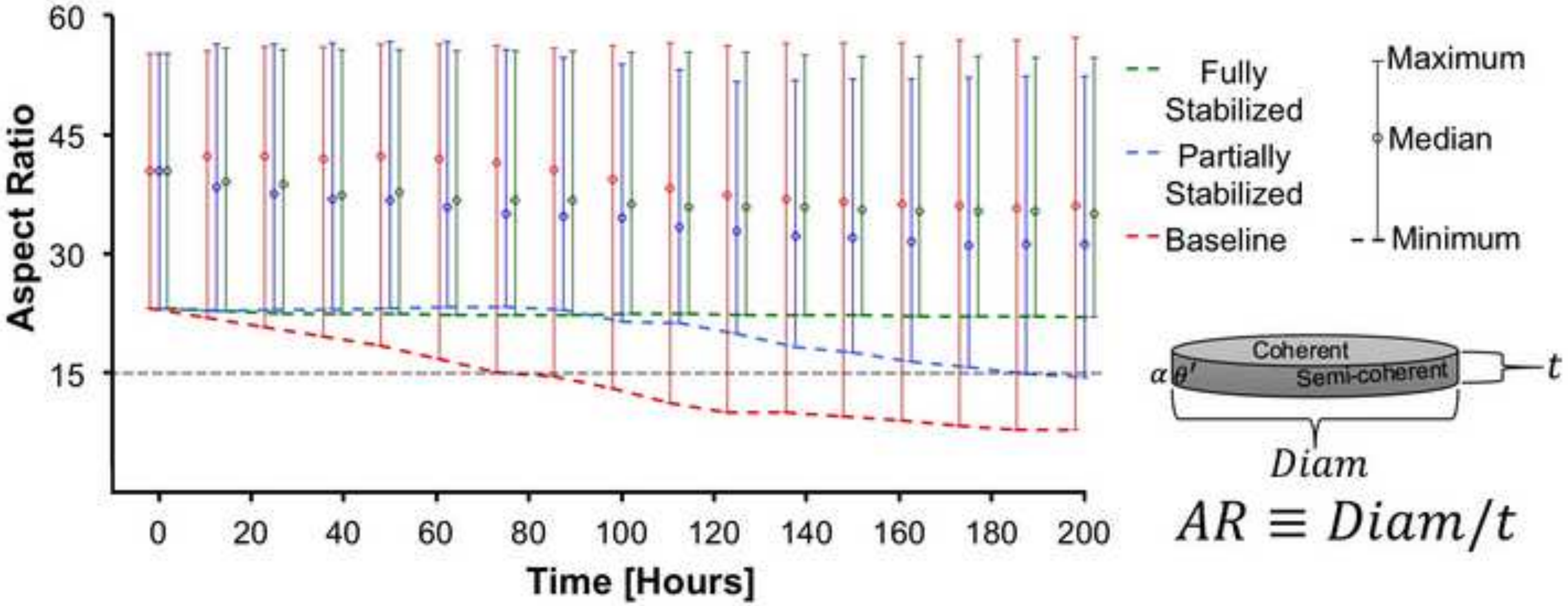
Aspect Ratio
60
45
30
15
0
20
40
60
80
100
120
140
160
180
200
Time [Hours]
Fully Stabilized
Partially Stabilized
Baseline
Maximum
Median
Minimum
Coherent
Semi-coherent
α
θ'
t
$Diam$
$AR \equiv Diam/t$

Figure 7

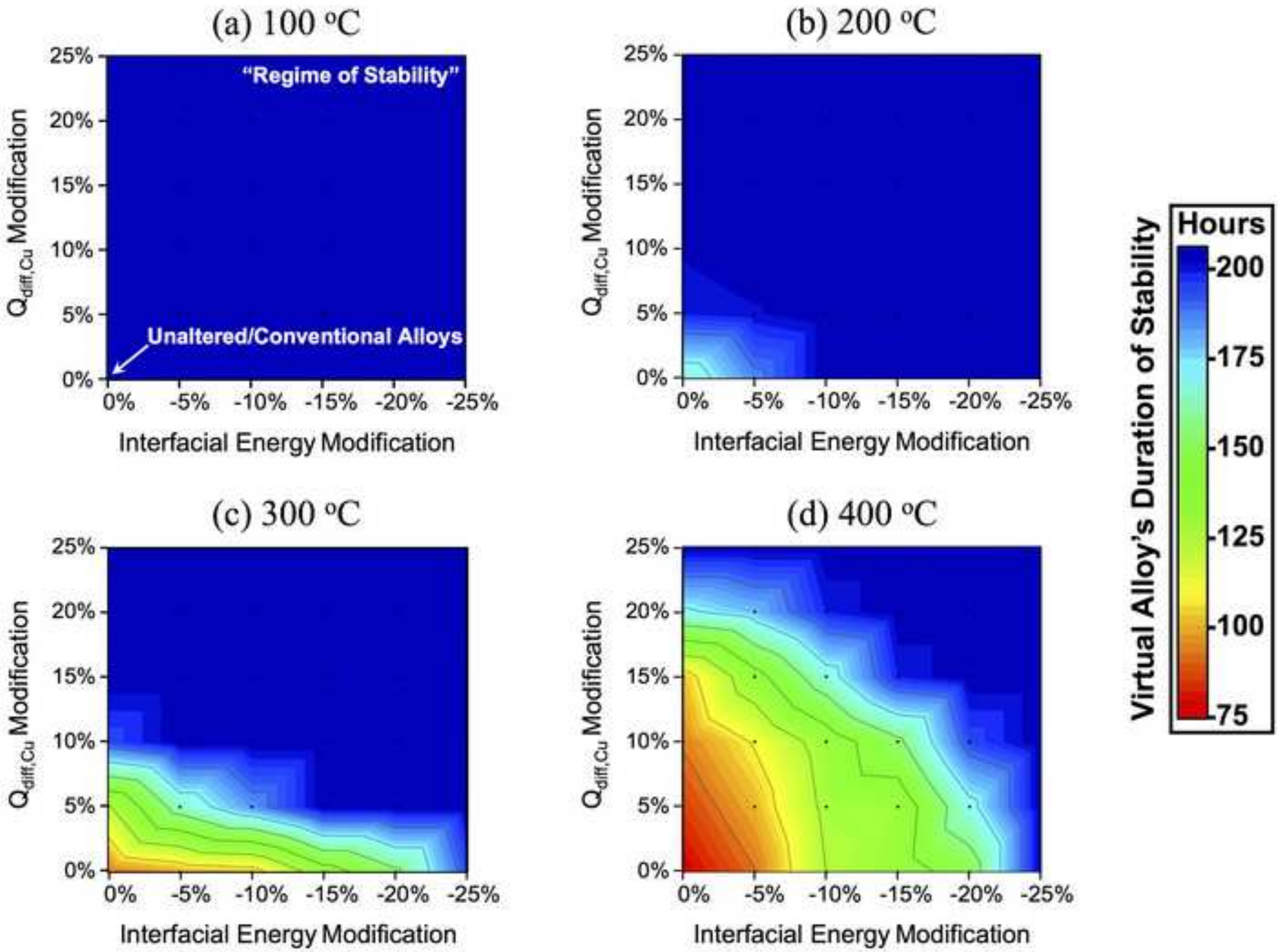
(a) 100 ºC
"Regime of Stability"
Unaltered/Conventional Alloys
(b) 200 ºC
(c) 300 ºC
(d) 400 ºC
25%
20%
15%
10%
5%
0%
0%
-5%
-10%
-15%
-20%
-25%
$Q_{diff,Cu}$ Modification
Interfacial Energy Modification
Virtual Alloy's Duration of Stability
Hours
200
175
150
125
100
75

Figure 8

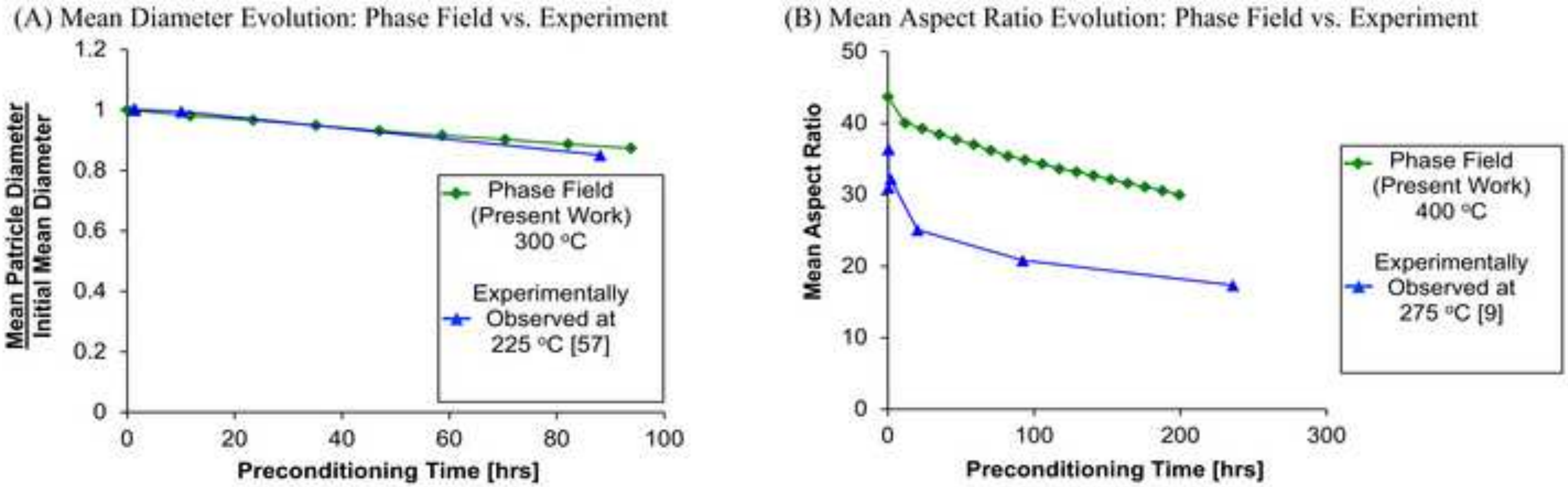

(A) Mean Diameter Evolution: Phase Field vs. Experiment

(B) Mean Aspect Ratio Evolution: Phase Field vs. Experiment

Figure 9

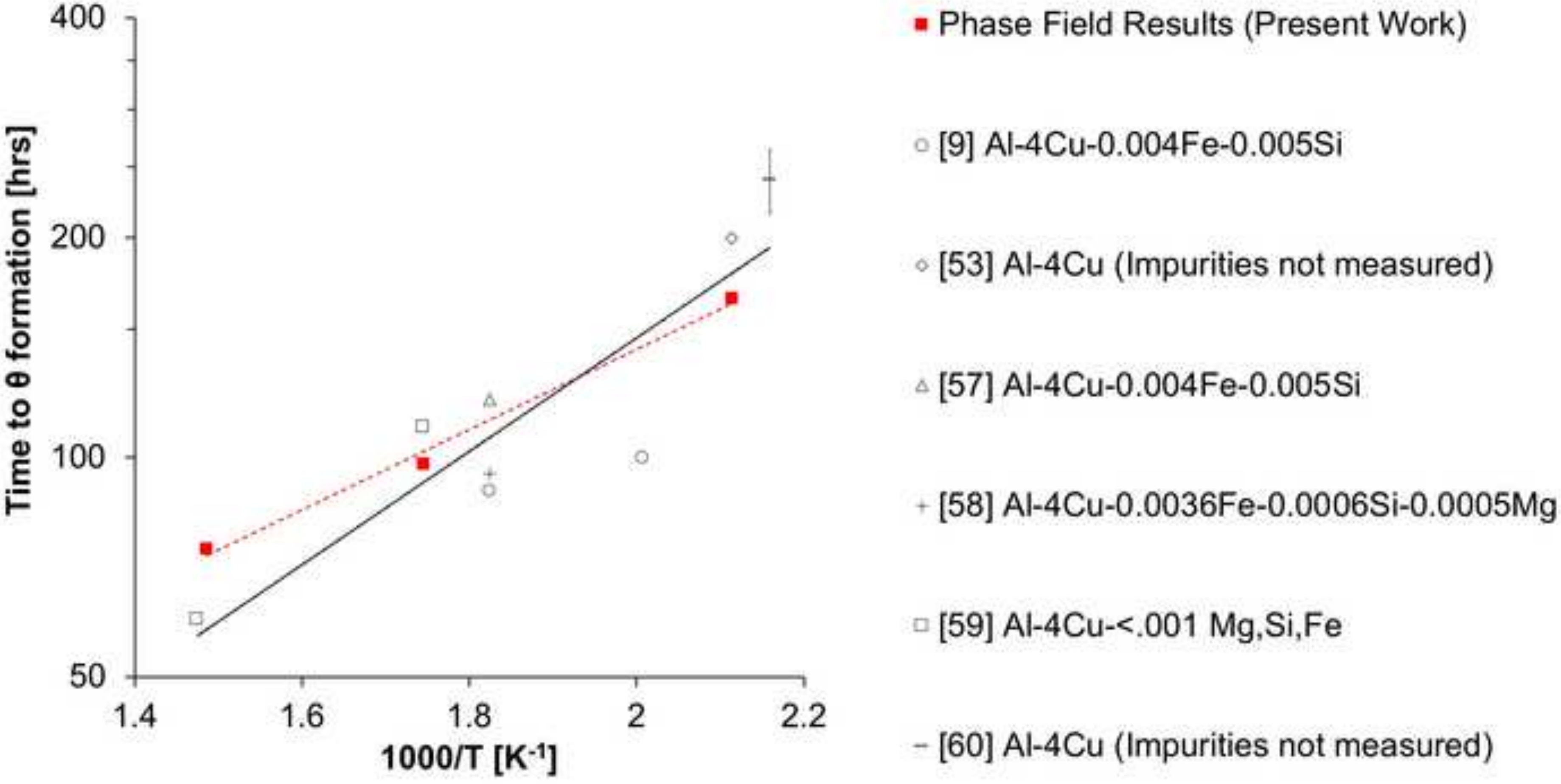
400
200
100
50
Time to θ formation [hrs]
1.4
1.6
1.8
2
2.2
1000/T [K-1]
Phase Field Results (Present Work)
[9] Al-4Cu-0.004Fe-0.005Si
[53] Al-4Cu (Impurities not measured)
[57] Al-4Cu-0.004Fe-0.005Si
[58] Al-4Cu-0.0036Fe-0.0006Si-0.0005Mg
[59] Al-4Cu-<.001 Mg,Si,Fe
[60] Al-4Cu (Impurities not measured)

Figure 10

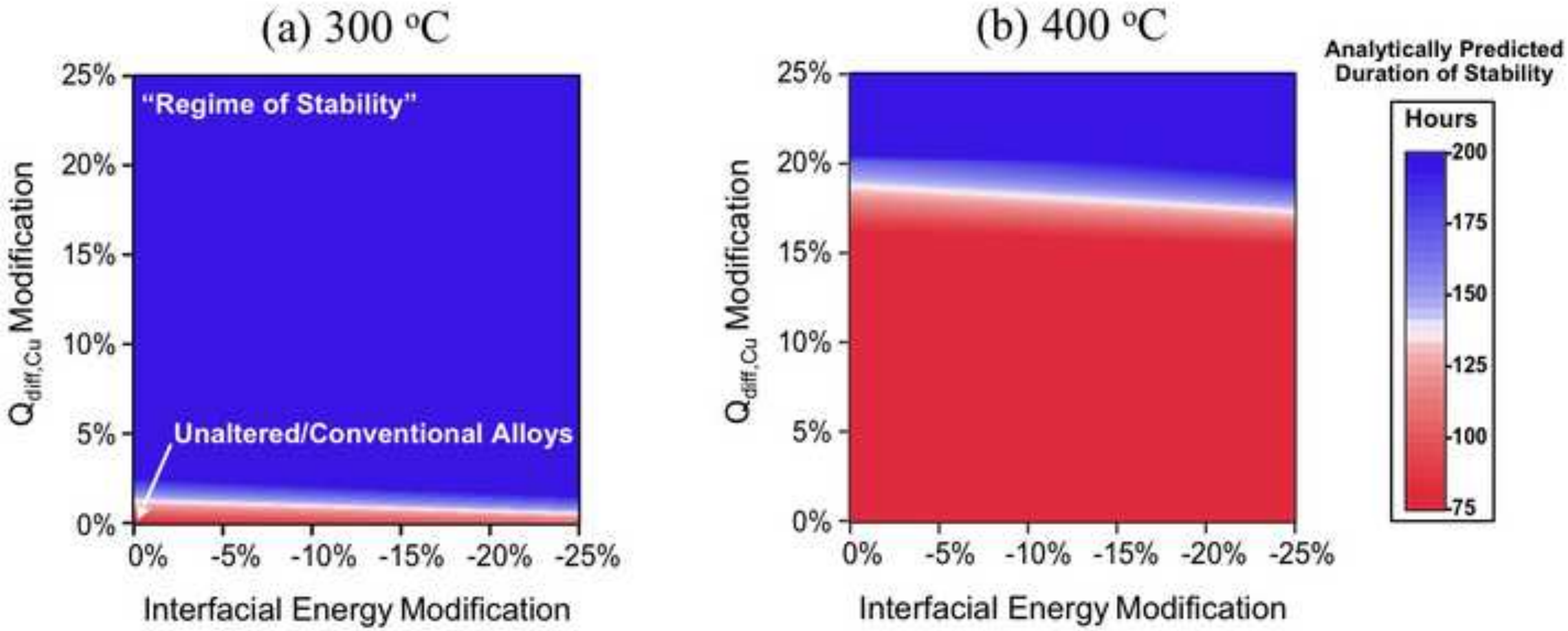
(a) 300 °C
(b) 400 °C
"Regime of Stability"
Unaltered/Conventional Alloys
$Q_{diff,Cu}$ Modification
Interfacial Energy Modification
25%
20%
15%
10%
5%
0%
0%
-5%
-10%
-15%
-20%
-25%
Analytically Predicted Duration of Stability
Hours
200
175
150
125
100
75

Figure 11

Click here to download high resolution image

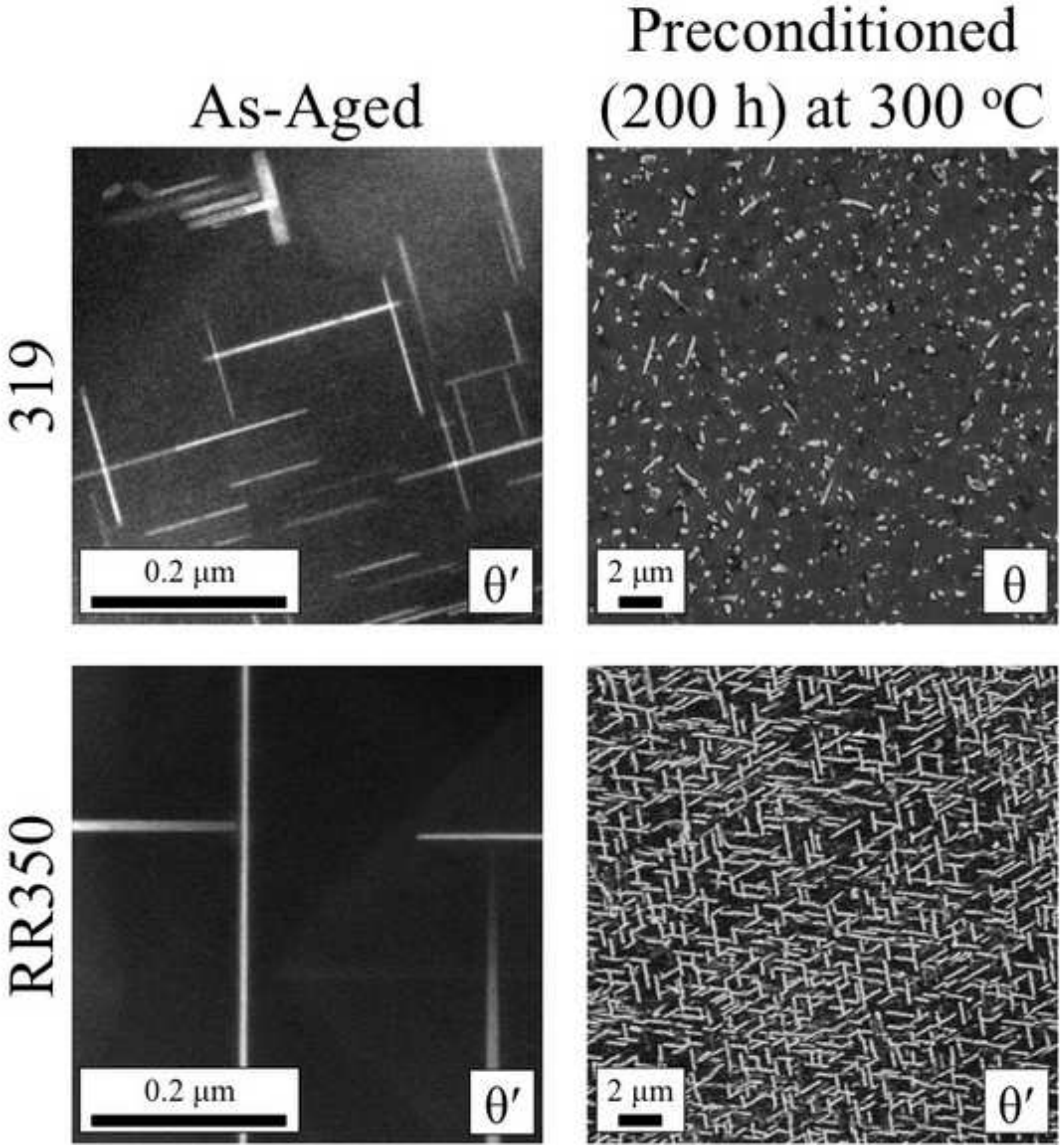

Tables in Word

Table 1.

Temperature	Function	a	b	c	d	e	h	j
100 °C	f_{α}					$2.450 \cdot 10^{2}$	$1.225 \cdot 10^{0}$	$-2.995 \cdot 10^{0}$
	$f_{\theta'}$	$1.336 \cdot 10^{6}$	$1.929 \cdot 10^{6}$	$1.144 \cdot 10^{6}$	$3.562 \cdot 10^{5}$	$6.196 \cdot 10^{4}$	$5.913 \cdot 10^{3}$	$2.621 \cdot 10^{2}$
200 °C	f_{α}					$2.815 \cdot 10^{2}$	$1.408 \cdot 10^{0}$	$-3.829 \cdot 10^{0}$
	$f_{\theta'}$	$2.260 \cdot 10^{6}$	$3.259 \cdot 10^{6}$	$1.929 \cdot 10^{6}$	$6.000 \cdot 10^{5}$	$1.037 \cdot 10^{5}$	$9.581 \cdot 10^{3}$	$3.824 \cdot 10^{2}$
300 °C	f_{α}					$3.300 \cdot 10^{2}$	$1.650 \cdot 10^{0}$	$-5.338 \cdot 10^{0}$
	$f_{\theta'}$	$2.270 \cdot 10^{6}$	$3.272 \cdot 10^{6}$	$1.937 \cdot 10^{6}$	$6.024 \cdot 10^{5}$	$1.041 \cdot 10^{5}$	$9.607 \cdot 10^{3}$	$3.805 \cdot 10^{2}$
400 °C	f_{α}					$3.270 \cdot 10^{2}$	$1.635 \cdot 10^{0}$	$-7.364 \cdot 10^{0}$
	$f_{\theta'}$	$2.299 \cdot 10^{6}$	$3.314 \cdot 10^{6}$	$1.962 \cdot 10^{6}$	$6.100 \cdot 10^{5}$	$1.053 \cdot 10^{5}$	$9.689 \cdot 10^{3}$	$3.772 \cdot 10^{2}$

Table 2.

Parameter	Value
$\gamma_{\mathrm{coherent}}$	$1.610 \left[\frac{\mathrm{eV}}{\mathrm{nm}^2}\right]$ [3]
$\gamma_{\mathrm{semi-coherent}}$	$3.289 \left[\frac{\mathrm{eV}}{\mathrm{nm}^2}\right]$ [3]
$\kappa_{\eta,\mathrm{coherent}}$	$4.128 \left[\frac{\mathrm{eV}}{\mathrm{nm}}\right]$
$\kappa_{\eta,\mathrm{semi-coherent}}$	$10.290 \left[\frac{\mathrm{eV}}{\mathrm{nm}}\right]$
κ_{Cu}	$3.826 \left[\frac{\mathrm{eV}}{\mathrm{nm}}\right]$

Table 3.

	Elastic moduli of α and θ′ [GPa]									
	FCC α Aluminum				Tetragonal θ′					
	c11	c12	c44		c11	c33	c44	c66	c12	c13
100 °C	101.0	59.8	26.0		178.8	169.7	28.0	44.2	72.0	75.3
200 °C	99.8	58.8	25.7		176.8	167.0	27.6	43.4	72.0	73.9
300 °C	95.6	57.8	24.1		174.8	164.3	27.3	42.6	72.0	72.6
400 °C	91.3	56.8	22.5		172.8	161.7	27.0	41.8	72.0	71.2

Table 4.

$Q_{diff,Cu}$ Modification	$Q_{diff,Cu}$ [kJ/mol]	Mobility at 100 °C [nm^2/sec]	Mobility at 200 °C [nm^2/sec]	Mobility at 300 °C [nm^2/sec]	Mobility at 400 °C [nm^2/sec]
0%	136	1.25E-07	1.32E-03	5.51E-01	3.82E+01
+5%	143	1.40E-08	2.35E-04	1.32E-01	1.13E+01
+10%	150	1.56E-09	4.17E-05	3.17E-02	3.36E+00
+15%	156	1.74E-10	7.40E-06	7.61E-03	9.98E-01
+20%	163	1.95E-11	1.31E-06	1.83E-03	2.96E-01
+25%	170	2.18E-12	2.33E-07	4.39E-04	8.79E-02

Table 5.

$\gamma_{\text{semicoherent}}$ Modification	$\gamma_{\text{semicoherent}}$ [mJ/m^2]	$\gamma_{\text{semicoherent}}$ [eV/nm^2]	$\kappa_{\eta,semicoherent}$ [eV/nm]
0%	560	3.289	10.29
-5%	532	3.125	9.69
-10%	504	2.960	9.08
-15%	476	2.796	8.48
-20%	448	2.631	7.88
-25%	420	2.467	7.27

Table 6.

Symbol	Definition	Value	Justification
AR_o	Initial Aspect Ratio	26	Minimum initial aspect ratio of a particle present in the simulations, and the most likely to reach the critical value of 15 first.
AR_{eq}	Equilibrium Aspect Ratio	2.04	Ratio of $\gamma_{semicoherent}$ to $\gamma_{coherent}$ shown in the supplementary file.
V	Precipitate volume	$7.49 \times 10^{-24}\ [m^3]$	Volume of a disc with the diameter and thickness of the minimum initial aspect ratio particle present in the simulations.
V_m	Molar Volume of θ′	$2.85 \times 10^{-5}\ [m^3]$	From the literature [57].
$x_{Cu,\alpha}$	Cu content far from θ′	$.25\ [atomic\ \%]$	Typically observed Cu content in matrix of θ′ strengthened alloys.
$x_{Cu,\theta'}$	Cu content of θ′	$33.33\ [atomic\ \%]$	From stoichiometry.
D_{Cu}	Diffusivity of Cu in Al	$D_{o,Cu} \cdot e^{-\frac{Q_{diff,Cu}}{R \cdot T}}$	Calculated for each temperature/ $Q_{diff,Cu}$ combination using parameters given in the supplementary file.
$\gamma_{semicoherent}$	Interfacial energy of semi-coherent interface	Varies	Values given in the supplementary file.
α	Ratio between the width of the Cu diffusion field and θ′ ledge height	201.7	Ledge height of 0.29 nm (minimum value observed, half of c value for θ′ unit cell), diffusion field of 58.5 nm (median radius of θ′ from data in Figure 4, as suggested by Merle *et al.* [57]).
λ	Spacing between ledges	$117\ [nm]$	Median diameter of θ′ from data in Figure 4, as suggested by Merle *et al.* [57]).

***Declaration of Interest statement**

Declaration of interests

☒ The authors declare that they have no known competing financial interests or personal relationships that could have appeared to influence the work reported in this paper.

☐The authors declare the following financial interests/personal relationships which may be considered as potential competing interests: